공학석사 학위논문

High-resolution Observation of Nucleation and Growth Behavior of Nanomaterials on Graphene

고분해능 관찰을 통한 그래핀 위에서의

나노물질의 초기성장단계 분석

2014년 2월

서울대학교 대학원

Department of Materials Science and Engineering

조 장 현

High-resolution Observation of Nucleation and Growth Behavior of Nanomaterials on Graphene

지도 교수: 김 미 영

이 논문을 공학석사 학위논문으로 제출함
2014년 2월

서울대학교 대학원
Department of Materials Science and Engineering
조 장 현

조장현의 석사 학위논문을 인준함
2014년 2월

위 원 장   남 기 태   (인)

부위원장   김 미 영   (인)

위   원   이 규 철   (인)

Abstract

High-resolution Observation of Nucleation and Growth Behavior of Nanomaterials on Graphene

Janghyun Jo

Department of Materials Science and Engineering

College of Engineering

Seoul National University

Studying nucleation and growth has been one of the major goals in materials science. Fundamental understanding of initial growth is essential for fabrication of nanomaterials with desired physical properties. Consequently, atomic level investigation on as-grown nuclei and local atomic arrangements around defects is required. Such high-resolution study along with crystallographic analysis could be performed using transmission electron microscopy (TEM). Here, we report on atomic-resolution observation of initial growth behavior using TEM by growing nanomaterials directly on graphene. Graphene exhibiting excellent electron beam transparency and high mechanical strength is an ideal supporting layer for TEM measurements by minimizing the

background signal from the underlying membrane. In addition to merely sustaining nanomaterials as a support, graphene can be further used as a substrate for nanomaterials growth. The crystalline nature of graphene along with its electron beam transparency ultimately enables direct imaging of nanomaterials and allows us to systematically investigate the initial growth mechanisms.

Using "direct growth and imaging" method, we could clearly observe the initial states of Zinc oxide (ZnO) nanomaterials. This enabled the observation of the transition in crystal structure of ZnO nuclei along with their orientational relationship with graphene. Furthermore, formation of various defects during nanomaterial growth could be clearly visualized with atomic-resolution. More generally, we believe that this simple technique may be readily expanded to investigate the growth mechanisms of many other nanomaterials on various two-dimensional layered substrates.

Contents

List of Tables

List of Figures

over time. BF images (**a,c,e,g**) were obtained, along with their corresponding SAED patterns (**b,d,f,h**) for ZnO grown for (a,b) 10 s, (c,d) 2 min, (e,f) 5 min, and (g,h) 15 min, respectively. These BF images show distinct characteristics of growth behavior occurring at each growth time, such as nucleus creation and growth, coalescence, and defect formation. The insets of e are FFTs obtained from HR-TEM images of Regions 1, 2, and 3, showing different in-plane orientation among coalesced clusters. The dashed lines and small circles in g denote low-angle grain boundaries and threading dislocations, respectively. In the SAED patterns, the changes in crystallinity of ZnO with respect to graphene are presented for each growth time. The main diffraction peaks of graphene and ZnO are marked with yellow circles and green arrows, respectively; an 800-nm-diameter aperture was used. …………..48

Figure 4.3   Non-epitaxially grown ZnO clusters in the initial growth stage. HR-TEM image of ZnO clusters grown for 2 min and the FFTs obtained from different ZnO clusters. Each position is identified by dashed squares 1, 2, and 3 in the image. In the FFTs, the diffraction peaks of ZnO $\{10\bar{1}0\}$ and graphene $\{10\bar{1}0\}$ are marked with green and yellow circles, respectively. All of the graphene $\{10\bar{1}0\}$ peaks in 1–3 were located at the same positions, whereas the ZnO $\{10\bar{1}0\}$ peaks exhibited various in-plane orientations at each position, with epitaxial relationships of 0°, 30°, and 11° with respect to graphene…...49

Figure 4.4   Moiré fringes (patterns) observed within ZnO clusters (or grains) during the coalescence process. **a,** HR-TEM image showing rotational Moiré patterns between two different ZnO clusters with a rotation angle of 11.4°. Insets 1, 2, and 3 are corresponding FFTs obtained from Regions 1, 2, and 3. **b,** Higher magnification BF image of Figure 2c. Moiré fringes are clearly shown within the ZnO clusters located on the underlying pre-formed ZnO layers. The Moiré fringes are marked with yellow arrows, and their spacing is ~ 12.1 Å. **c,** HR-TEM image of the grain boundary for ZnO grown for 10 min.

Chapter 1. Introduction

1.1 Importance of studying the initial growth behavior of nanomaterials

A nanostructure is an object which has the size of nanometer scale, especially less than 100 nm. Nanostructures can be classified into three categories according to the number of dimensions on the nanoscale; nanoparticles and nanodots (or quantum dots) belong to zero-dimensional nanostructures having three dimensions on the nanoscale; nanowires and nanorods belong to one-dimensional nanostructures having two dimensions on the nanoscale; nanowalls and thin films belong to two-dimensional (2-D) nanostructures having one dimension on the nanoscale (Fig. 1.1). Many researches have been devoted to artificially fabricating these nanostructures using various method, such as vapor-liquid-solid and chemical vapor deposition (CVD), and notable achievements have been widely reported as shown in Fig 1.2.[1]

The development of growth technique and the realization of fabricating various nanostructures by bottom-up approach have greatly increased the versatility of electronic and optoelectronic device applications (Fig. 1.3).[2-5] The various kinds of nanostructures feature their distinctive physical properties, which is a key point in expanding their applicability to

more diverse technology. Such a variety of physical properties of nanostructures mostly arise from their structural characteristics. For example, controlling the shape of a plasmonic nanoparticle gives rise to tailoring and fine-tuning its optical resonance properties.[6] Low-dimensional semiconductor structures, such as nanowire, quantum well, and quantum dot, also exhibit a lot of extraordinary properties related to quantum size effect, in electronic transport and light emission.[7,8] In addition, the defect structures and dopants in semiconductor can greatly alter the electrical and optical properties of the matter.[9,10] These structural characteristics of nanostructures are mostly determined by the initial growth behavior; thus studying nucleation and growth, including how nuclei are formed and how they evolve into nanomaterials, is one of the most important topics in materials science.[11-13]

Atomic-scale studies are essential for the detailed understanding of the initial growth mechanisms, occurred on the order of a few nanometers, and the fabrication of nanomaterials having desired characteristics.[14-17] Observation of the arrangements of atoms in as-grown nuclei would enable us to investigate the growth mechanism such as cluster nucleation and evolution of the nuclei.[18] This tells us which crystal structure these nuclei have and which specific site they choose to grow at. In addition, atomic-resolution imaging offers the information on how the grain growth and the electrical properties of the

materials are affected by dopants and impurities within grains or grain boundaries at the initial state. Moreover, distorted atomic arrangements at the dislocation cores and grain boundaries would provide the additional information about the physical properties of the matter, such as the electrical property across the grain boundary.[19]

Scanning electron microscopy (SEM) is an efficient tool for investigating the evolution of nanomaterials; however, it gives only limited information on the nucleation and growth process. The resolution of SEM is not suitable for the analysis of individual nuclei, and SEM cannot provide information on the crystal structure of the nanomaterials.[20,21] Additionally, the epitaxial relationship with respect to the substrate, important for the study of heteroepitaxial growth, cannot be obtained using SEM. Scanning tunneling microscopy (STM) has been also widely used to study surface structure at the atomic scale[22]; 0.1 nm lateral resolution and 0.01 nm depth resolution can be achieved. However, STM has a limited scanning area, and its application requires conducting surfaces that are extremely stable and clean, which lessens its applicability to the initial growth study of various nanomaterials. For this reason, high-resolution transmission electron microscopy (HR-TEM), providing crystallographic as well as atomic-resolution information, could be the best experimental tool for the versatile analysis of the nucleation and initial

growth of nanomaterials.[12,23,24] (See the comparison between SEM and TEM in Table. 1.1)

It is, however, important to note that the destructiveness of the conventional TEM sampling process makes it difficult to probe nanomaterials at the atomic scale. Several steps employed in the preparation of TEM samples, such as mechanical polishing, focused ion milling, and sonication, may introduce serious damages causing amorphization, modification and disintegration of the crystal structure of nanomaterials.[25] Several attempts to overcome this problem were tried by directly growing nanocrystals on prefabricated thin membranes such as a-carbon[26], Si_3N_4[27], and SiO_2[28]. However, poor electron transmittances of the membranes arising from their thickness of a few tens of nanometers caused blurred images and made it difficult to conduct atomic-resolution imaging of the nanocrystals clearly. In addition, amorphous characteristic of the membranes is not suitable as a substrate for crystal growth, thus they cannot be used for studying initial growth behavior of nanomaterials.

Here, we report on atomic-resolution observation of initial growth behavior using TEM by growing nanomaterials directly on graphene. Graphene, which has excellent electron beam transparency and high mechanical strength, was used as both a substrate for nanomaterials growth and a supporting layer for TEM measurements. Crystalline nature of graphene along with its electron

beam transparency ultimately enables the direct growth and imaging method. The direct imaging of evolution of nanomaterials on graphene without any additional sampling processes allowed us to examine details of the initial growth behavior with atomic-resolution and high sensitivity. We chose Zinc oxide (ZnO) as the growth material because it has recently been used for novel electronic and optoelectronic device applications.[2,3,5,29] Using this technique, we could clearly observe the initial states of ZnO nuclei and their structural changes, evolution of heteroepitaxial growth, and arrangements of atoms in defects with atomic-resolution.
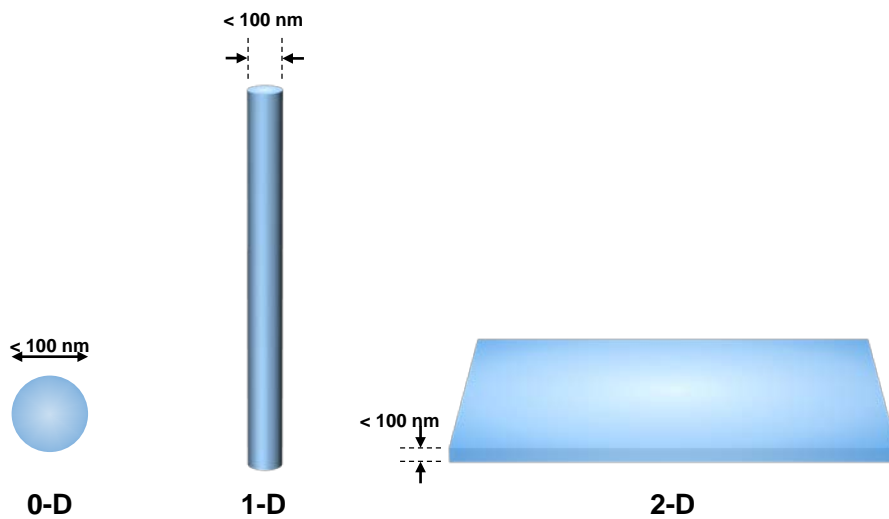
Figure 1.1 | Schematics of nanostructures having various shapes. The nanostructures are classified as 0-D, 1-D, 2-D according to the number of dimensions on the nanoscale.
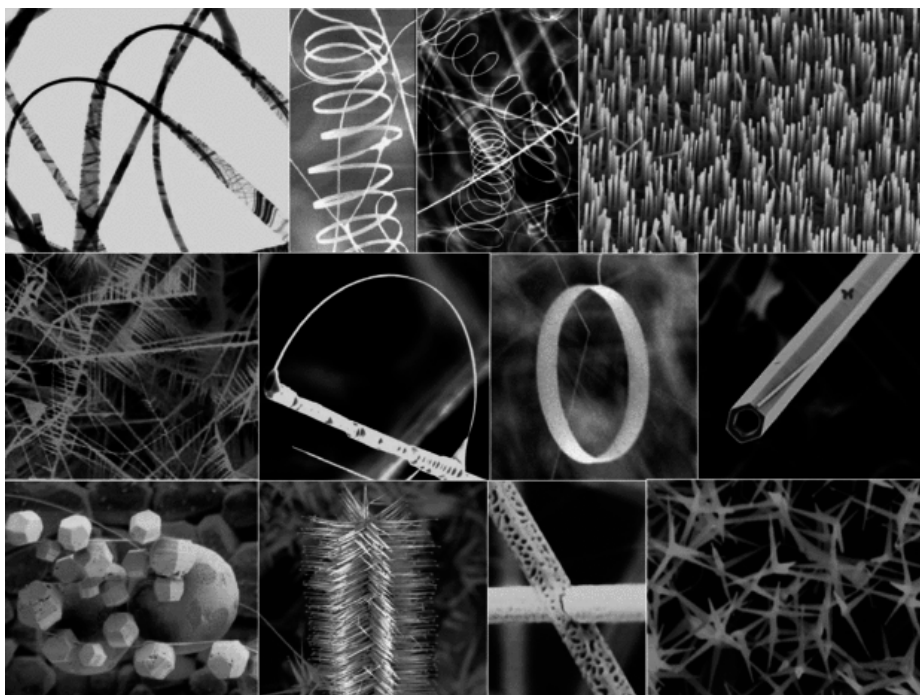
Figure 1.2 | A collection of ZnO nanostructures. The figures show nanodots, nanorods, nanowires, nanobelts, nanotubes, nanobridges and nanonails, nanowalls, nanohelixes, seamless nanorings, mesoporous single-crystal nanowires, and polyhedral cages.[1]
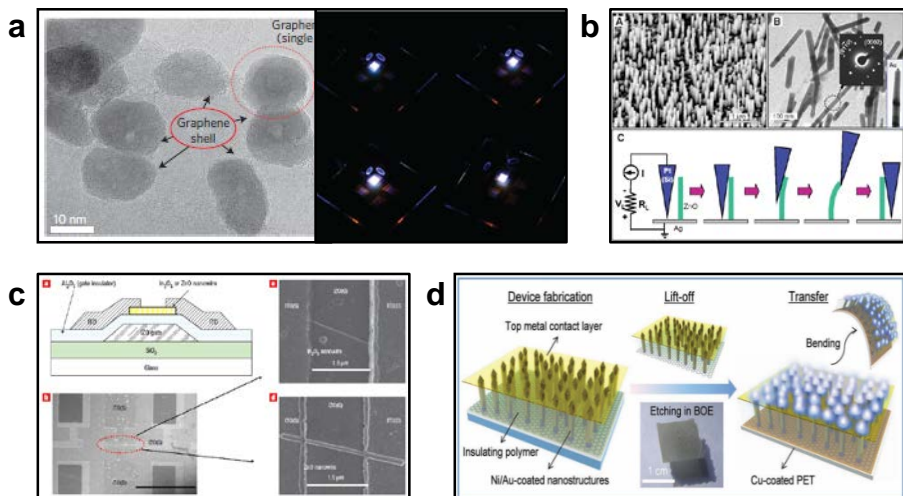
Figure 1.3 | Various kinds of ZnO nanostructures and their applications to electronic and optoelectronic devices. a, ZnO-graphene quantum dot for white-LED.[5] **b,** Piezoelectric nanogenerators based on ZnO nanowire arrays.[2] **c,** Transparent nanowire transistors for transparent and flexible electronics.[3] **d,** GaN/ZnO coaxial nanorod heterostructures grown on graphene for flexible LED.[4]

8
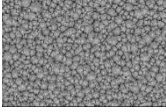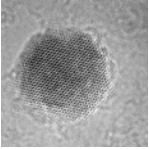
	Emission/ Imaging source	Available information from image	Accelerated voltage	resolution	Image
SEM	Electron gun/ Secondary or backscattered electron	Surface morphology	A few ~ a few tens of kV	~ a few nm	
TEM	Electron gun/ Transmitted electron	Projected 2-D image and lattice image (at high-resolution)	100 kV ~ a few MV	~ Å	

Table 1.1 | Comparison of the operation and performance between SEM and TEM imaging. With SEM, we can only observe the surface morphology of the sample, whereas the lattice image and crystallographic information can be further obtained by TEM measurements.

1.2 Materials of interest

1.2.1 ZnO

ZnO has been investigated for a long time as a "promising material"
for the application to electronic and optoelectronic devices owing to its
remarkable properties and potential to be fabricated in various forms of
nanostructures as shown in Fig. 1.2. ZnO has three types of crystal structures,
wurtzite, zinc blende, and rock-salt. Unit cells of these ZnO polymorphs is
shown in Fig. 1.4. Of these structures, wurtzite structure is the commonest in
nature because of its structural stability arising from minimum total energy.[30]
This ZnO wurtzite structure has a hexagonal unit cell with two lattice
parameters, a and c, in the ratio of c/a=1.633 and belongs to the space group of
P63mc.[30]

ZnO which has a wide band gap possesses excellent physical
properties including high quantum efficiency, optical transparency, large
breakdown voltage, and large exciton binding energy. These properties provide
benefits for ZnO to be applied in optoelectronics, transparent electronics, and
spintronics.[30] First, ZnO with a direct band gap can achieve high quantum
efficiency. An electron transition can take place between conduction band and
valence band in a direct band gap only with an aid of photon energy whereas
momentum transfer should occur in the case of indirect transition. This

indicates that electron transition in the band structure of ZnO takes place more easily without generating or annihilating phonons. This property introduces high quantum efficiency of ZnO and offers advantages over other materials in the optoelectronics such as light-emitting diode.[31] Optical transparency of ZnO is attributed to its wide band gap (E_g~3.3 eV at 300 K)[30] which is outside the range of visible light spectrum. This feature makes ZnO a promising material for the transparent optoelectronic device in the future.[3] Meanwhile, large breakdown voltage of ZnO allows it to sustain large electric fields, and also large voltage. Breakdown voltage is a parameter of a diode that defines the largest reverse voltage that can be applied without causing an exponential increase in the current in the diode. Therefore, the large breakdown voltage gives rise to the better diode-like characteristics and enhances the performance of the diode. ZnO also has a large exciton binding energy of ~60 meV[32,33] that is substantially larger than that of ZnSe (22 meV) and GaN (25 meV) which have been widely researched as a light-emitting materials.[34] The exciton binding energy of ZnO is about 2.4 times that of the thermal energy at room temperature ($K_B T$=25 meV) resulting in an intense near-band-edge excitonic emission by exciton recombination at room and even higher temperatures. This explains strong luminescence of ZnO at room temperature. Besides, ZnO has piezoelectric properties arising from its intrinsic polarization inside the material.

This feature allows ZnO to be a candidate for energy saving device by changing mechanical energy to electrical energy, and vice versa.

1.2.2 Graphene

Graphene is a one-atom thick layer whose structure consists of sp^2-bonded carbon atoms that are densely packed in a honeycomb crystal lattice. Because of its atomic-scale thickness, graphene exhibits optical transparency. Figure 1.5a shows a regular hexagonal array of carbon atoms in graphene layer. Monolayer graphene was first isolated by Geim and colleagues in 2004 by the mechanical exfoliation method.[35] They used adhesive tape to repeatedly peel away graphite into flakes of layered graphene, and eventually produced single layer of graphene. Figure 1.5b reveals photograph of graphene flakes transferred on top of an oxidized Si wafer by scotch tape method.[35]

Graphene possesses remarkable electrical and thermal properties, compared with other traditional materials. These characteristics is attributed to the linear dispersion relation of graphene at low energies near the six corners of the 2-D hexagonal Brillouin zone, as represented in Fig. 1.5c.[36] This unusual feature of graphene gives rise to zero effective mass for electrons and holes, called massless Dirac fermions, which are described by the (2+1)-D Dirac equation with an effective speed of light $v_F \sim 10^6 \ m \ s^{-1}$.[37] The massless Dirac

fermions in graphene feature ballistic transport without scattering process. High-quality graphene exhibits ballistic transport on the submicrometer scale even at room temperature (up to $0.3 \mu m$ at 300 K).[37] In other words, this ballistic transport in graphene significantly enhances its electrical and thermal properties.

Graphene is also one of the strongest materials in nature. Graphene exhibits extremely high mechanical strength; measurements have shown that graphene has a tensile strength of 1 TPa which is even greater than that of diamond and steel.[38] This high value of mechanical strength makes graphene strong and rigid. The excellent properties of graphene, including thermal conductivity, electron mobility, and tensile strength, are summarized in Table 1.2 with a comparison with other materials.
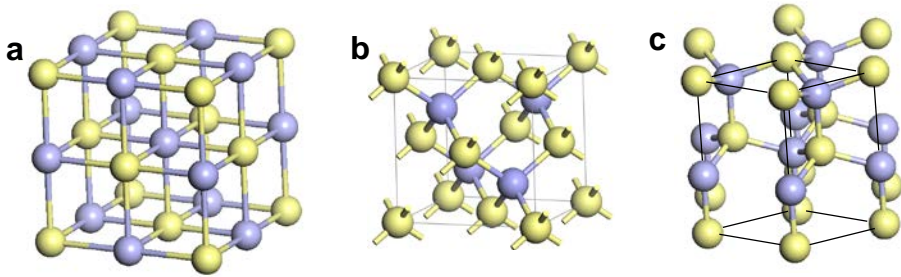
Figure 1.4 | Unit cells of ZnO polymorphs. a, Rock salt, **b,** Zinc blende, **c,**

Wurtzite.
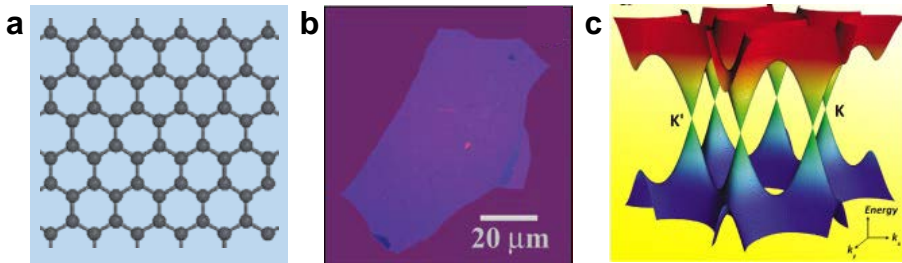
Figure 1.5 | The characteristics of graphene. a, Schematic of hexagonal arrays of carbon atoms in graphene. **b,** Photograph of mechanically exfoliated graphene layers transferred onto an oxidized Si wafer.[35] **c,** 3-D dispersion relation observed in graphene near the six Dirac points. The valence and conduction bands touch at the Dirac points, which makes graphene behave like a zero-band-gap semiconductor.[36]

	Thermal conductivity (at room Temp.) [W m^{-1} K^{-1}]	Electron mobility (at room Temp.) [cm^2 V^{-1} s^{-1}]	Tensile strength [GPa]
Graphene	4840 ~ 5300	up to 100000~200000 (without impurity)	1000
Other material	Silver	Silicon	Aluminum
	429	1400	69

Table 1.2 | The physical properties of graphene including thermal conductivity, electron mobility, and tensile strength with a comparison with other related materials.

Chapter 2. Literature Survey

2.1 Direct crystal growth on prefabricated thin membranes for TEM measurements

There have been many efforts to perform TEM measurements without sample preparation steps because these processes are time-consuming and may cause severe damage on the specimen, especially for fragile nanomaterials. In order to solve the problem, a method directly growing nanomaterials on prefabricated thin membranes was designed. The membrane generally consisted of a few tens of nanometers-thick-amorphous window, such as SiO_2 and Si_3N_4, suspended in a Si frame. Figure 2.1 shows a schematic of such a prefabricated thin membrane which was developed a few decade ago, but also has been widely used until now.[27,28] This membrane window fabricated by wet-etching allows electron-beam transmission, thus TEM image of nanomaterials placed on it can be obtained without additional TEM specimen preparation processes.

The direct observation method using prethinned membranes dates back a few decades. Enquist *et al.* fabricated an electron-beam transparent window to observe ultrathin porous metal films 3−40 nm thick using TEM.[28] To fabricate such a window, SiO_2 was vapor phase deposited onto polished front surface of Si wafer which was then anisotropically back-etched in a 35%

aqueous solution of KOH at 80˚C using nitride mask. These processes successfully allowed SiO_2 membrane to be suspended on the Si frame. Fig. 2.2a shows such a TEM membrane containing a SiO_2 window, 50−200 nm thick and 150×150 μm wide. Pt thin film was vapor phase deposited directly on this electron-beam transparent membrane and imaged by TEM without any further manipulation, as shown in Fig. 2.2b. Using this method, Enquist *et al.* was able to study ultrathin porous gate metals grown on the same substrate as used in real applications.

Grant *et al.* also obtained TEM images of nanoparticles, on the order of ten nanometers, using prefabricated thin membrane.[27] The membrane in Fig. 2.2c was also produced by the back-etch process using etchant solution, resulting in 40 nm-thick-Si_3N_4 window with the dimension of 100×100 μm. Using this membrane, Grant *et al.* studied detailed mechanisms of protein absorption onto non-biological surfaces to demonstrate feasibility of the electron-beam transparent window for TEM measurements. Figure 2.2d reveals iron-containing protein (ferritin) nanoparticles absorbed onto an oxidized TEM window.

Many other nanostructured materials have also been investigated using prefabricated thin membranes other than thin films or nanoparticles. Nucleation and growth mechanisms of carbon nanotubes (CNTs) were studied

18

by Verissimo *et al.* to obtain the knowledge of the basic parameters, such as diameter and chirality, associated with the whole process of CNTs synthesis.[39] In this study, electron-beam transparent multi-layer membranes were exploited for the characterization of CNTs by TEM. These membranes consisted of amorphous carbon films 20 nm thick and SiO_2 support layer 30 nm thick, as shown in Fig. 2.2e. Afterward, metal catalyst was deposited on top of the multi-layer membranes, and CNTs were grown by the conventional catalytic CVD process. Figure 2.2f shows CNTs grown on multi-layer membranes with elongated metal catalysts. Verissimo *et al.* verified that such metal catalysts were liquefied during the multi-wall CNTs nucleation. Similar work using Si_3N_4 membrane was also reported to investigate the high-quality single-walled CNTs with a broad diameter distribution.[40] Gu *et al.* synthesized CNTs with a microcontact-printing method (Fig. 2.2g), and the resulting single-walled CNTs were imaged in Fig. 2.2h.

The ultrathin window has also been exploited even in liquid cells for in-situ TEM measurements in recent years. Zheng *et al.* used liquid cell reactor which seals chemical solutions within two Si_3N_4 windows 25 nm thick and 1×25 µm wide (Fig. 2.2i).[41] The liquid cell was installed to a special TEM sample holder, and chemical reaction such as colloidal nanocrystal growth was visualized in real time. With this liquid cell, Zheng *et al.* observed Pt

nanocrystal growth induced by electron beam irradiation in solution in real time, as shown in Fig. 2.2j. This technique enables tracing nanocrystal growth trajectories and understanding the fact that coalescence process significantly contributes to nanocrystal growth.
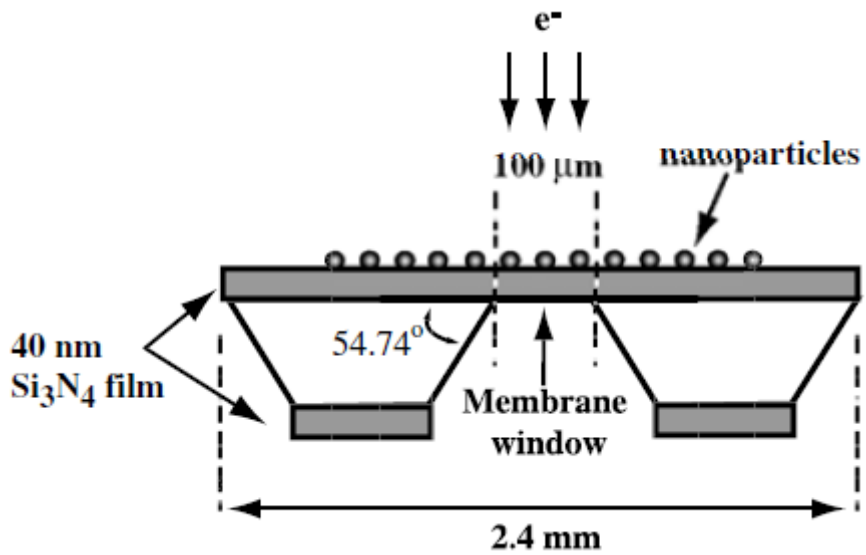
Figure 2.1 | Schematic of the side view of the prefabricated thin membranes.

Electron beam can transmit through the membrane window back-etched by etchant solution, which enables producing TEM images of the nanomaterials placed on the membrane window.[27]
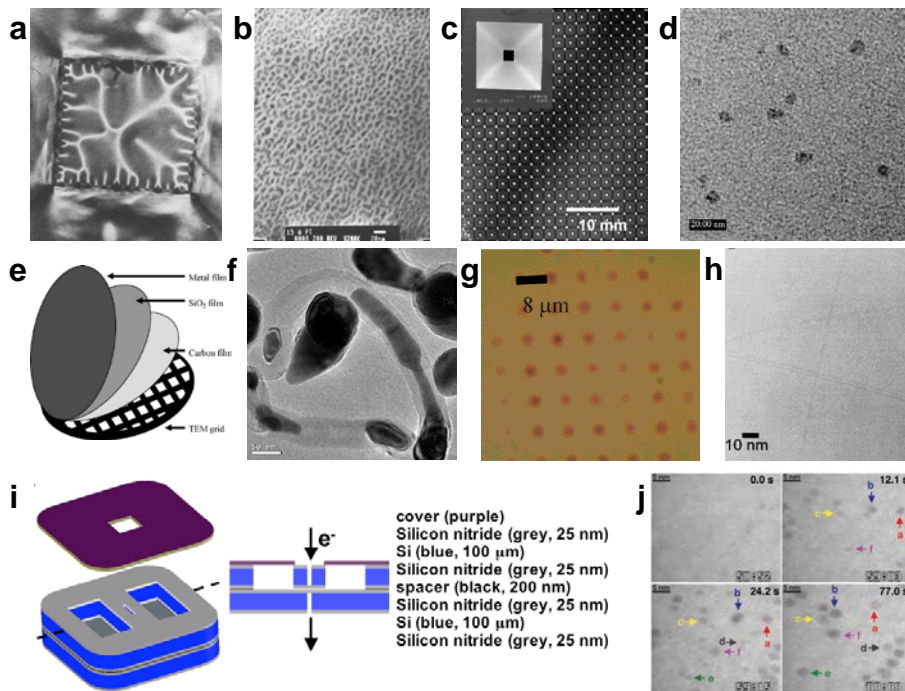
Figure 2.2 | Prefabricated TEM membranes and TEM images obtained by corresponding membranes. a, Photograph of SiO_2 window suspended in a Si frame.[28] **b,** TEM image of Pt film 1.5 nm thick grown on a membrane a. **c,** Optical microscope (OM) image of a membrane containing ~300 Si_3N_4 windows. Inset shows an SEM image of an electron-beam transparent window.[27] **d,** TEM image of ferritin particles on a membrane c. **e,** Schematic of multi-layer membranes containing SiO_2 and amorphous carbon layers.[39] **f,** TEM image of CNTs and metal catalysts on a membrane e. **g,** OM image of 20 nm-thick-Si_3N_4 membrane with metal catalyst islands.[40] **h,** TEM image of single-walled CNTs grown on a membrane g. **i,** Schematic of TEM liquid cell sealed with two electron-beam transparent Si_3N_4 windows.[41] **j,** TEM image of Pt nanocrystals crystallized by electron beam irradiation in the liquid cell e acquired at different growth times.

22

2.2 Graphene as a supporting layer for TEM measurements

Recently, graphene has been used as a TEM sample support for imaging nanoparticles because of its remarkable physical properties. Excellent electron beam transparency of graphene minimizes the background signal from the underlying graphene membrane. In addition, High mechanical strength of graphene enables sustaining nanoparticles even in free-standing condition. These advantages of graphene eliminate the need for using additional thick-supporting layer to sustain graphene, which facilitated clear atomic-resolution imaging of the nanoparticles supported by atomically thin graphene. Additionally, remarkable electrical and thermal conductivity of graphene also minimize charging and heating effects under electron beam irradiation during TEM measurements.

2-D layered materials generally exhibit electron-beam transparency owing to their atomically thin characteristic, as mentioned above. These 2-D crystallites were first introduced by Geim with the method of mechanical exfoliation.[35] A fresh surface of a layered materials were exfoliated by scotch tape or rubbed against another surface, which left a variety of thin flakes attached to them. Figure 2.3a shows the graphene flake made by such a rubbing process, which leads to the formation of a few layers graphene, confirmed by

atomic force microscopy (AFM). The electron-beam transparency can be also anticipated from many other 2-D materials exhibiting their intrinsic thin characteristic, as shown in Fig. 2.3b.

Graphene has advantages over many other 2-D layered materials as an electron-beam transparent membrane for TEM measurements because it consists of low-atomic-number element, namely carbon (Z=6). Such materials composed of light element scatter incident electrons less than those with heavy elements, thus allowing to image objects very clearly without background effects. Figure 2.3c shows such an electron-beam transparent graphene supported by etched Si microchip.[42] We can verify that graphene layers did not make a big difference on the contrast in TEM image although contrast difference was conspicuous in the regions of folded graphene (right side of Fig. 2.3c). In addition, the graphene remained its structure with a relatively large area laterally even in a free-standing region. These characteristics of graphene enable exploiting it as an ideal supporting layer for TEM measurements.

The previous studies which reveal feasibility of using graphene as a supporting layer for TEM measurements are briefly demonstrated in Fig. 2.3d-f. Figure 2.3d shows how graphene was practically used as a supporting layer for TEM measurements.[43] Graphene was transferred onto a holey carbon TEM grid by the method of mechanical cleavage with an adhesive tape. Graphene

24

suspended over the perforated regions of amorphous carbon layer appeared exceptionally clean without dramatic contrast in the image. This suspended area of graphene thus would be used to observe various kinds of nanomaterials.

With these characteristics of graphene, Meyer *et al.* visualized individual low-atomic-number adatoms on single-layer graphene, and investigated their dynamics in real time.[43] Here, graphene membrane offered high-sensitivity with respect to the adatoms, allowing the visualization of even ultra-low-contrast objects using conventional TEM. They summed 100 consecutive TEM frames for the same physical region (Fig. 2.3e), and compared the images to simulations to rule out any adatom heavier than He, as well as a substitution of carbon atoms in the graphene membrane by other elements. This process confirmed that the grey and dark contrast marked with red and black arrows in Fig. 2.3e were hydrogen and carbon adatoms, respectively. Meanwhile, graphene membrane was also used to study soft-hard interfaces, such as nanoparticles functionalized with organic molecules (Lee *et al.* 2009).[44] Graphene was synthesized in the gas phase using a substrate-free, atmospheric-pressure microwave plasma reactor. Using this graphene, Lee *et al.* observed the fine structure of citrate coating and the citrate-gold nanoparticles interface with an aid of aberration-corrected TEM, as shown in Fig. 2.3f. The use of graphene in this study facilitated direct atomic-resolution

image of the surface molecules and interface on a nanoparticle for the first time. Furthermore, this method expanded the scope of research to the field where conventional TEM experiments could not be applied, including the observation of nanoparticles functionalized with a diverse range of molecular coatings such as DNA, proteins, and antibody/antigen pairs.

More recently, graphene was even exploited to observe the crystallization in liquid in real time (Yuk *et al.* 2012).[17] In general, gas or liquid phase reaction was not able to be observed in electron microscopy since the equipment should be kept at extremely high vacuum. Reaction cell composed of a few nanometers-thick-windows has been mostly used to isolate reactive materials from the rest part of the electron microscopy. However, this reaction cell was not suitable for the atomic-resolution imaging using TEM due to significant electron-beam scattering arising from its thick windows. Yuk *et al.* solved this problem by using electron-beam transparent graphene for encapsulating gas or liquid materials for ambient- and vacuum-condition experiments. High flexibility, mechanical tensile strength, and impermeability of graphene allows the use of graphene as a reaction cell. In this study, solution of Pt nanocrystals was isolated between two graphene layers, so-called graphene liquid cell (Fig. 2.4a), and Pt nanocrystals were crystallized by electron beam irradiation. The graphene liquid cell enabled observing various

26

process of crystallization, such as shape evolution and coalescence of Pt nanocrystals (Fig. 2.4b), with high-resolution.

Liquid cell using graphene window has also been used for in-situ SEM measurements. Stoll *et al.* observed colloidal Au nanoparticles dispersed in water using the graphene liquid cell and showed the feasibility of this cell for in-situ SEM analysis.[45] The graphene liquid cell used in this study is schematically illustrated in Fig. 2.4c. Colloidal Au nanoparticles were encapsulated within the commercial stainless steel orifices having laser drilled pinholes with diameters between 2 and 10 µm, which was covered by graphene and pressure relief membrane. Both incident and secondary electrons passed through the graphene window on top of the stainless frame, thereby enabling SEM imaging. Figure 2.4d shows SEM image taken with this experimental equipment, which reveals the transparency of graphene window.
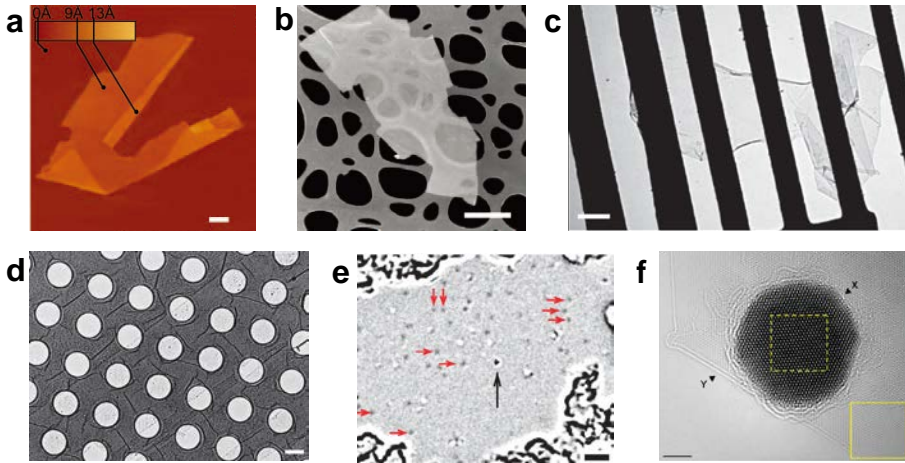
Figure 2.3 | Graphene membranes as a supporting layer for nanoparticles observation by TEM. a, AFM image of multi-layer graphene on oxidized Si wafer.[46] **b,** SEM image of $Bi_2Sr_2CaCu_2O_x$ 2-D crystal on a holey carbon film.[46] **c,d,** Bright-field TEM image of a suspended graphene membrane on a etched Si substrate and perforated amorphous carbon layer, respectively.[42,43] **e,** Hydrogen (red arrows) and carbon (black arrow) adatoms on graphene.[43] **f,** an atomic-resolution image of a gold nanoparticle and its surrounding citrate capping agent placed on the graphene membrane.[44] Scale bar: (a,b) 1 μm, (c) 500 nm, (d) 1 μm, (e,f) 2 nm.

28
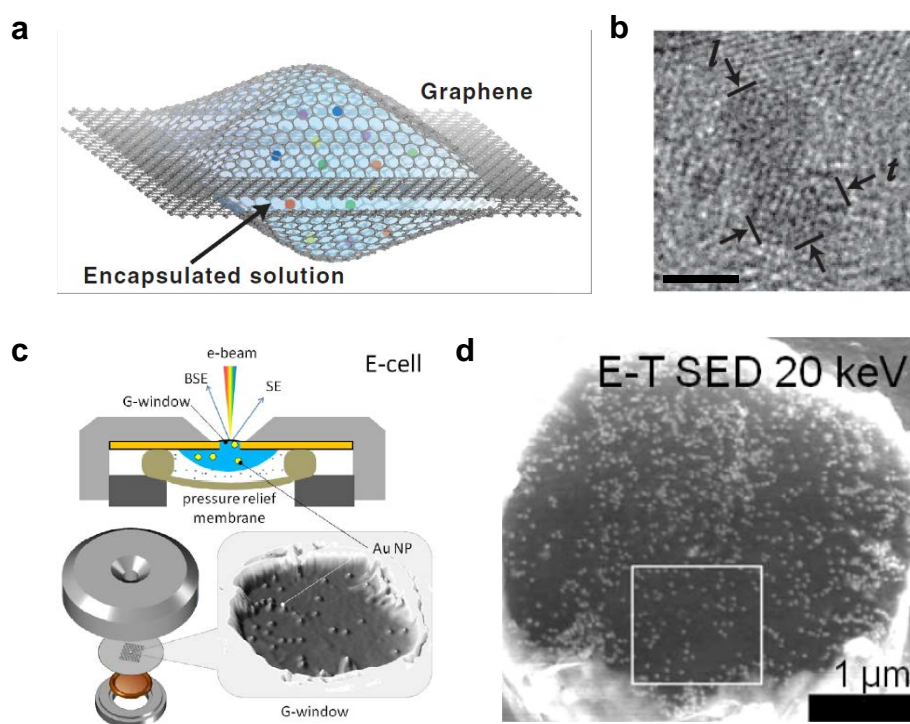
Figure 2.4 | Graphene cells encapsulating liquid phase materials for in-situ electron microscopy. a, Schematic of the graphene liquid cell containing growth solution of Pt nanocrystals.[17] **b,** Atomic-resolution image of coalescence between two Pt nanocrystals in graphene liquid cell. Scale bar: 2 nm. **c,** Schematic of the graphene liquid cell encapsulating Au nanoparticles colloidally suspended in water. The real SEM image on the right shows Au nanoparticles underneath the graphene.[45] **d,** SEM image of graphene liquid cell filled with colloidal Au nanoparticles suspended in water.

Chapter 3. Experimental method

The experimental procedures in this study are divided into four parts: the first part is the growth of graphene by CVD method, the second part is the transfer of graphene onto a TEM grid, the third part is the growth of ZnO nanomaterials by metal-organic CVD (MOCVD), the fourth part is the characterization of the ZnO nanomaterials using SEM and TEM, and the last part is the First principles calculations about the structural stability of ZnO polymorphs. Overall experimental procedures are shown schematically in Fig. 3.1.

3.1 Growth of CVD graphene

Graphene was grown on copper foil (25-μm-thick, Alfa Aesar) using CVD furnace. Schematic of the furnace for CVD graphene growth are shown in Fig. 3.2. After copper foil was cut into small pieces and cleaned with acetone and methanol, a quartz boat containing copper foil was loaded at the hot zone of a tube furnace. Before the growth, copper foil was annealed at 1000°C for 30 min with employing only hydrogen as an ambient gas. During the growth process, methane gas was injected into the reactor, with hydrogen as the carrier gas. Growth was carried out at 1000°C for 30 min, and the reactor pressure was kept at 150−200 Torr. Detailed growth conditions of CVD graphene are

described in Table 3.1.

3.2 Transfer of CVD graphene onto a TEM grid

After graphene growth, poly(methyl methacrylate) (PMMA) was spin-coated onto graphene and baked at 140˚C for 90 s. Then the graphene layers on the other side of the copper foil was removed by oxygen plasma treatment. To separate graphene from the copper foil, it was etched away using a solution of ammonium persulfate ($(NH_4)_2S_2O_8$) (0.04 g mL^{-1}). Afterward, PMMA-supported graphene floating in the solution was rinsed using deionized water and carefully lifted by TEM grids (Quantifoil holey carbon grid, acquired from Ted Pella). The graphene transferred on TEM grids were then dried using hot plate at ~110˚C for 15 min. The graphene was then immersed in acetone to remove the PMMA coating, resulting in only graphene remaining on the TEM grids.
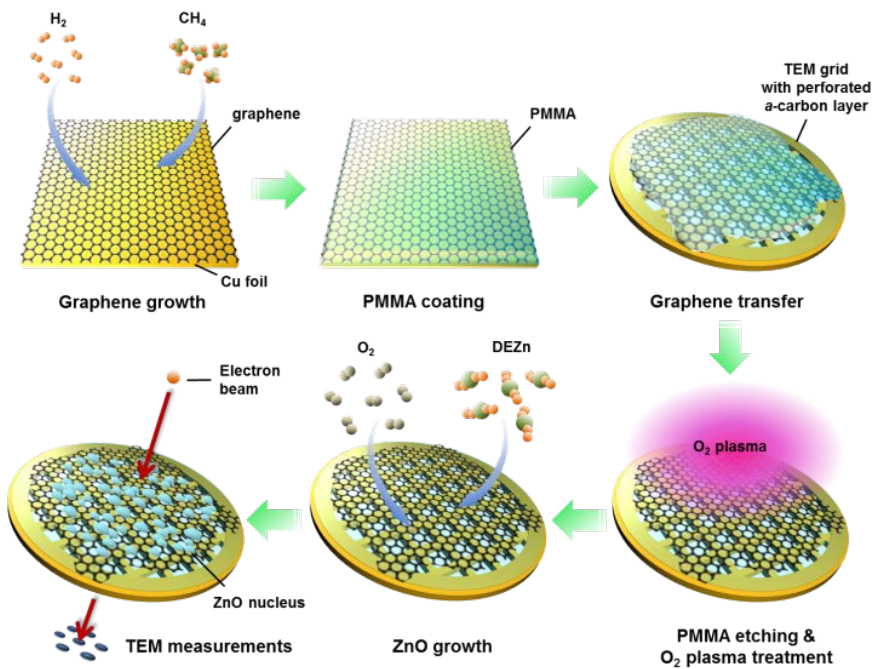
Figure 3.1 | Schematic diagram of the experimental technique for growing ZnO nanomaterials on graphene and performing TEM measurements. In this schematic diagram, the experimental method used in this research is introduced step by step. Graphene was grown by CVD method and then transferred onto a TEM mesh grid with a perforated amorphous carbon layer to make a simple experimental system. The graphene surface was exposed to oxygen plasma to enhance nucleation. Then, ZnO nanomaterials were grown on the plasma-treated graphene by MOCVD and observed using TEM. No additional TEM specimen preparation process, such as manual grinding or ion milling, was carried.
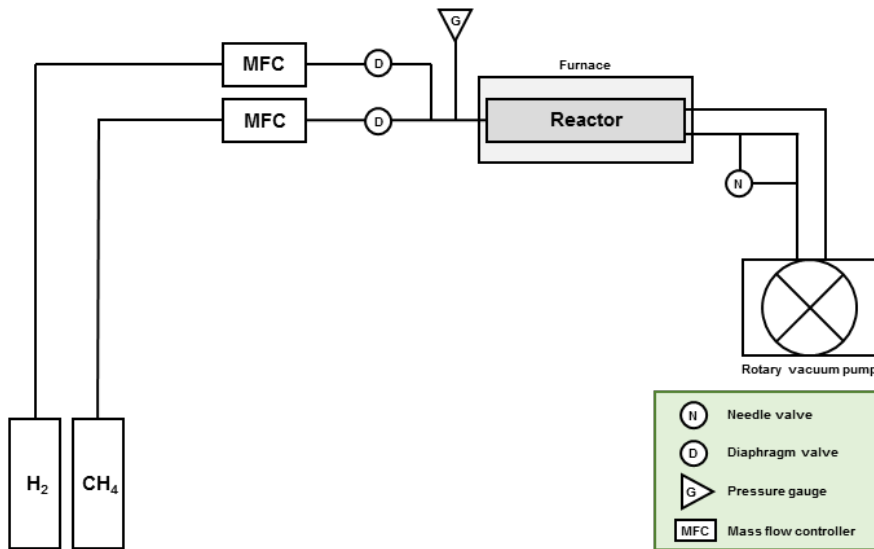
Figure 3.2 | Schematic of the CVD furnace system. For graphene growth,

CH_4 was employed as the reactant gas and H_2 was used as a carrier gas.

	Growth conditions
Substrate	Copper foil
Reactor pressure	150−200 Torr
Growth temperature	1000˚C
Growth time	30 min
Anneal time	30 min
CH_4 flow rate	35 sccm
H_2 flow rate	100 sccm

Table 3.1 | Typical growth conditions of CVD graphene.

3.3 Growth of ZnO nanomaterials on graphene placed on a TEM grid

The surface of graphene transferred on TEM grids was treated with oxygen plasma for 3 s to enhance the nucleation sites over the whole area. Afterward, the TEM grid with graphene layers was loaded into the MOCVD reactor, and ZnO nanomaterials were directly grown on graphene using catalyst-free MOCVD for various growth times (10 and 30 s, and 1, 2, 5, 10, and 15 min). Schematic of the MOCVD system for ZnO nanomaterials growth are shown in Fig. 3.3. Diethylzinc and oxygen gas were injected into the reactor, with argon as the carrier gas. The reactor temperature was raised to 580−600°C, and the pressure was kept at ~2 Torr during the growth process. Detailed growth conditions of ZnO nanomaterials are given in Table 3.2.

3.4 Structural characterization of ZnO nanomaterials
3.4.1 SEM

The morphology of the ZnO nanomaterials on graphene which were grown by the method described in 3.3 was characterized using a field-emission SEM instrument (Carl Zeiss–AURIGA). In-lens secondary electron detector is equipped to this SEM for high-resolution and contrast imaging. The acceleration voltage was set to 2 kV with a working distance of ~3.8 mm to

observe the surface morphology of nanomaterials clearly.

3.4.2 TEM

To investigate the crystal structure and epitaxial relationship of ZnO nanomaterials with graphene, bright-field (BF) and high-resolution images, along with selected area electron diffraction (SAED) data, were obtained with a 200-kV field-emission TEM instrument (FEI Tecnai F20 and JEOL 2100F). SAED patterns were taken within a hole in the underlying amorphous carbon layer to eliminate the electron-beam scattering effect from that layer. In addition, only single crystalline regions of graphene were considered, with an aperture of 800 nm in diameter, for SAED analysis to study the epitaxial relationship between ZnO and graphene. Crystal structures of ZnO nanomaterials were investigated by analyzing the fast Fourier transform (FFT) patterns of the high-resolution images.
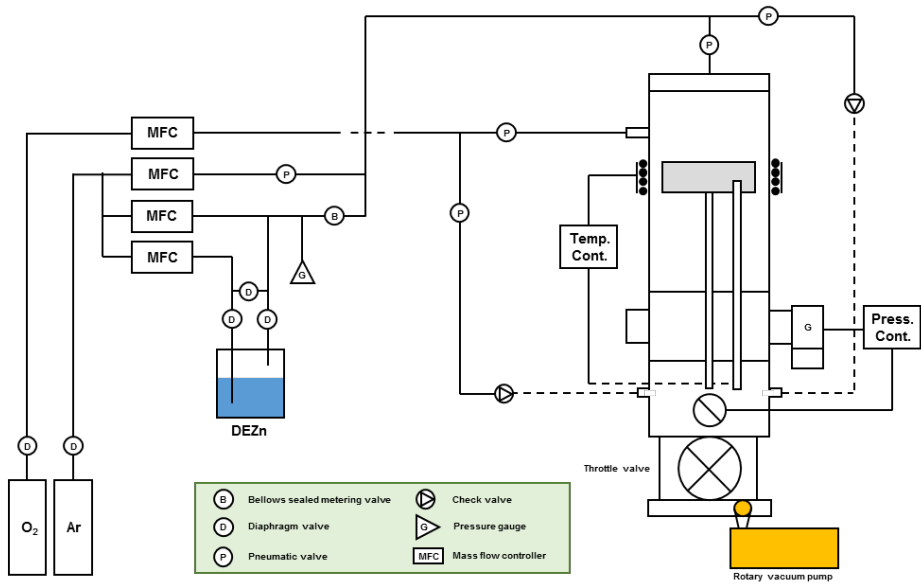
Figure 3.3 | Schematic of the vertical ZnO MOCVD system. For ZnO nanomaterial growth, DEZn and O_2 were employed as the reactant gases and Ar was used as a carrier gas.

	Growth conditions
Substrate	Graphene
Reactor pressure	~ 2 Torr
Growth temperature	580−600˚C
Growth time	10 sec / 30 sec / 1 min / 2 min / 5 min / 10 min / 15 min
DEZn flow rate	20 sccm
DEZn dilute flow rate	40 sccm
O2 flow rate	100 sccm
Ar flow rate	1500 sccm
Bubbler temperature of DEZn	−15˚C

Table 3.2 | Typical growth conditions of ZnO nanomaterials.

3.5 First principles calculations

The first principles calculations based on the density functional theory (DFT) was carried out to compare the total energy of the ZnO and GaN phases: wurtzite, zincblende, and rocksalt. All of the calculations were performed with the Vienna ab initio simulation package code, in which the projector augmented wave potential was used to describe the interaction between ions and electrons; the generalized gradient approximation was used for the exchange-correlations functional. Plane-wave basis sets were used with a plane-wave cutoff of 500 eV. For relaxation of the atomic positions, atoms were allowed to move until the forces on each atom were below 0.01 eV Å^{-1}. Brillouin-zone integrations were carried out on a grid of 20×20×20 Monkhorst–Pack special points for the zincblende and rocksalt phases and 24×24×16 Monkhorst–Pack special points for wurtzite.

Chapter 4. Results and discussions

4.1 Feasibility of the experimental technique for ZnO growth and TEM measurements

To confirm the thermal, mechanical, and chemical stability of the graphene/TEM grid system as a template for nanomaterial growth at high temperatures, various analysis tools including OM, SEM, and TEM were used. The TEM grid and graphene withstood high temperatures and retained their overall shape during the growth process, as shown in Fig. 4.1a and b. Although surface roughness of the graphene/amorphous carbon layer was observed, OM images clearly showed that graphene and the underlying perforated amorphous carbon layer still existed (Fig. 4.1b, inset). These findings revealed that the system remained in fairly good condition, even after the high-temperature growth process. Additionally, the robustness of this system indicated that the subsequent characterizing steps, such as TEM, could be performed without introducing damage to the ZnO/graphene system.

SEM was performed on the perforated region of the amorphous carbon layer, which showed graphene with ZnO nanomaterial (Fig. 4.1c). The SEM image indicated that free-standing graphene could be obtained due to its high mechanical strength and additionally that the ZnO nanomaterial grew on the graphene in this system in the same manner as they did on conventional

graphene using arbitrary substrates. This ensured that the system could be exploited to investigate the general growth behavior of ZnO on graphene.

The feasibility of TEM observation in the region of free-standing graphene was also verified. Graphene minimizes electron beam scattering due to its thinness and low atomic number; thus, TEM experiments could be conducted without additional sample preparation processes that inevitably caused severe damage to the specimen, especially on fragile nanomaterials. Background signal during ZnO nanomaterial imaging, which could possibly arise from the graphene supporting layers, were not evident in the TEM images, as shown in Fig. 4.1d. Additionally, ZnO nanostructures grown on free-standing graphene remained stable under the TEM conditions, indicating the suitability of our system for the investigation of the nucleation and growth mechanisms of ZnO on a graphene substrate.
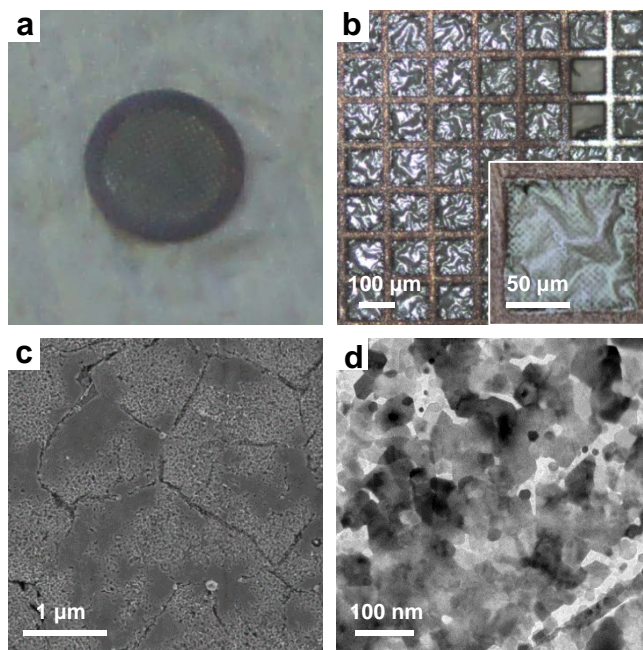
Figure 4.1 | Feasibility of using a graphene/TEM grid system for nanomaterial growth and TEM measurements. a, Photograph of the graphene/TEM grid system. This shows that the TEM grid maintained its structure after 15 min at 580°C. **b,** OM image of a TEM mesh grid. The inset is a magnified OM image of a TEM mesh, showing micrometer-sized holes with an amorphous carbon layer underneath the graphene. **c,** SEM image of ZnO nanomaterials on graphene. This image was taken within a hole in the amorphous carbon layer, showing ZnO nanomaterials growing on free-standing graphene. **d,** TEM image obtained over the region of free-standing graphene. This image exhibits a high contrast of ZnO nanomaterials with respect to the underlying graphene, which is completely invisible on the images, indicating the excellent suitability of graphene for this TEM study.

4.2 Overall growth behavior of ZnO nanomaterials on graphene

4.2.1 Nucleation and cluster growth stages

The morphological evolution of ZnO nanocrystals and their epitaxial relationship with graphene were studied at different growth stages using BF images and associated SAED patterns. As shown in Fig. 4.2a, isolated ZnO nuclei, a few nanometers in size, began to form on the graphene substrate in the initial 10 s of growth. At this nucleation stage, little crystallographic information of the ZnO nuclei could be obtained using SAED because of an insufficient amount of the crystalline ZnO phase (Fig. 4.2b). Figure 4.2c shows that ZnO nuclei gradually formed larger clusters, on the order of a few tens of nanometers, as the growth time increased. The growth of clusters in size was proceeded at the expense of the surrounding material, including the attached adatoms and aggregated adjacent nuclei.[41,47] The density of the ZnO clusters also increased due to the continuous formation of additional nuclei. Moreover, distinctive contrast due to thickness variation was observed within the ZnO clusters, which strongly suggests that ZnO clusters were formed by 3-D growth mode on graphene. This may be attributed to the chemical inertness of graphene, which inhibits prevalent nucleation of ZnO over the entire surface and causes preferable attachment of adatoms to nearby ZnO clusters. The SAED pattern in

Fig. 4.2d reveals dispersed diffraction peaks of ZnO clusters with the hexagonal phase (green arrows) around single-crystalline peaks of graphene (yellow circles). This indicates the presence of non-epitaxially-grown ZnO clusters in the initial stage, despite the overall tendency for epitaxial growth on graphene. The misorientation angles between clusters, determined by the positions of the diffraction peaks, were mostly smaller than 14°.

The non-epitaxial relationship between the ZnO clusters and graphene substrate at the early stages of growth was further investigated in detail. HR-TEM images and the corresponding FFTs were obtained for ZnO grown for 2 min, as shown in Fig. 4.3. Although graphene showed single-crystalline characteristics within the observed region, ZnO exhibited different in-plane orientations at each position. As indicated in the insets in Fig. 4.3, the crystal orientation of the ZnO clusters exhibited misorientation angles of 0°, 30°, and 11° with respect to that of graphene. The misorientation angles of 0° and 30° can be explained by the heteroepitaxial relationship between ZnO and graphene; it is energetically favorable when the $[10\bar{1}0]$ or $[11\bar{2}0]$ direction of ZnO matches the $[10\bar{1}0]$ direction of graphene. However, the misorientation angle of 11° obtained from Region 3 is not consistent with the heteroepitaxial relationship satisfying the most stable state. This shows that some of the ZnO clusters underwent non-epitaxial growth during the initial growth stage,

44

producing the dispersed diffraction peaks observed in Fig. 4.2d.

4.2.2 Postnucleation stages: coalescence

During the coalescence stages, there was a significant change in the overall orientational relationship of ZnO with graphene. Fig. 4.2e shows coalescence among the ZnO clusters, which occurred in 5-min-grown ZnO. These clusters often have the different in-plane orientations confirmed by FFTs in the insets of Fig. 4.2e, resulting in dispersed diffraction peaks, as shown in Fig. 4.2f, similar to those observed for the initial stage.

Rotational Moiré fringes (patterns) observed along the inclined boundary planes of the ZnO clusters (or grains) also provided additional evidence of coalescence among misoriented clusters. Figure 4.4a shows the rotational Moiré patterns observed along the boundary of ZnO clusters grown for 2 min. These hexagonal-shaped patterns resulted from different in-plane orientations of two clusters, which was confirmed by FFTs obtained from Regions 1, 2, and 3.

A BF image in Fig. 4.4b shows rotational Moiré fringes arising from ZnO clusters piled up at the boundary region. This indicates that the crystallographic orientation of the ZnO cluster on top differs from that of the cluster placed on the bottom. The misorientation angle between these two

clusters was 13°, as estimated by corresponding FFTs (Fig. 4.2e, inset 2), which was consistent with the 12.1-Å spacing of the Moiré fringes. The rotational Moiré fringe spacing (d_{rm}) can be calculated from the relationship;

$$d_{rm} = \frac{d}{2 \sin \beta/2} \qquad (1)$$

where d is a d-spacing of ZnO $(10\bar{1}0)$ plane and β is a rotation angle between the two clusters.

Meanwhile, the Moiré fringes were also observed along the grain boundary, as shown in the HR-TEM image in Fig. 4.4c. The Moiré fringes at the grain boundary indicated that both grains were tilted at the boundary and one of them was partly positioned on top of the other within the region showing the defective shape. Corresponding FFTs obtained from Regions 1, 2, and 3 reveal that each grain is single crystalline in structure, although they have different in-plane orientations. A set of parallel continuous streaks in Inset 2 is responsible for the structural disorder at the grain boundary. These FFTs from two different grains exhibited a misorientation angle of 21° between the ZnO grains, which is consistent with the 7.8-Å spacing of the Moiré fringes.

4.2.3 Postnucleation stages: formation of epitaxial relationship

After 15-min growth, the coalescence took place over the entire area, and ZnO clusters merged into larger grains, resulting in the formation of grain

boundaries (Fig. 4.2g). Meanwhile, the SAED pattern for such merged ZnO grains (Fig. 4.2h) showed the diffraction peaks having overall six-fold symmetry and misorientation angles smaller than 6°. Thus, ZnO and graphene exhibited an epitaxial relationship of ZnO $(10\bar{1}0)_h$ ∥ graphene $(10\bar{1}0)_h$ and ZnO $[0001]_h$ ∥ graphene $[0001]_h$.

The change of the in-plane orientation distribution of ZnO grains from 14° to 6° may be explained by growth competition between the grains at the grain boundaries. ZnO grains satisfying a well-matched epitaxial relationship with graphene have low interfacial energy. These ZnO grains grew dominantly during coalescence to minimize the interfacial energy of the system, thereby resulting in the formation of strong crystallographic alignment of the grains over the entire area. This postnucleation phenomenon, the occurrence of epitaxy by subsequent coalescence, might results from the chemical inertness of a graphene substrate.[48] The formation of a well-matched epitaxial relationship strongly suggests that graphene substrates affect the growth of ZnO during the entire initial growth process.
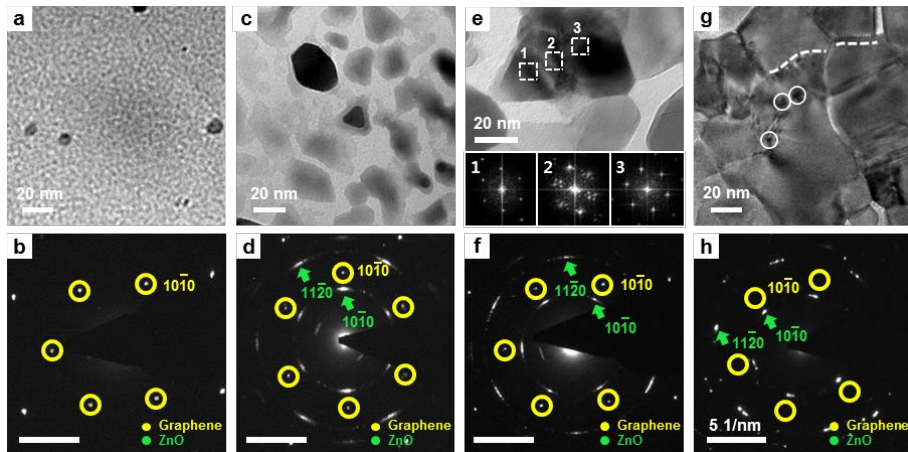
Figure 4.2 | Morphological evolution of ZnO nanomaterials on graphene and the gradual change of the epitaxial relationship between ZnO and graphene over time. BF images (**a,c,e,g**) were obtained, along with their corresponding SAED patterns (**b,d,f,h**) for ZnO grown for (a,b) 10 s, (c,d) 2 min, (e,f) 5 min, and (g,h) 15 min, respectively. These BF images show distinct characteristics of growth behavior occurring at each growth time, such as nucleus creation and growth, coalescence, and defect formation. The insets of e are FFTs obtained from HR-TEM images of Regions 1, 2, and 3, showing different in-plane orientation among coalesced clusters. The dashed lines and small circles in g denote low-angle grain boundaries and threading dislocations, respectively. In the SAED patterns, the changes in crystallinity of ZnO with respect to graphene are presented for each growth time. The main diffraction peaks of graphene and ZnO are marked with yellow circles and green arrows, respectively; an 800-nm-diameter aperture was used.

48

Figure 4.3 | Non-epitaxially grown ZnO clusters in the initial growth stage.

HR-TEM image of ZnO clusters grown for 2 min and the FFTs obtained from different ZnO clusters. Each position is identified by dashed squares 1, 2, and 3 in the image. In the FFTs, the diffraction peaks of ZnO $\{10\bar{1}0\}$ and graphene $\{10\bar{1}0\}$ are marked with green and yellow circles, respectively. All of the graphene $\{10\bar{1}0\}$ peaks in 1–3 were located at the same positions, whereas the ZnO $\{10\bar{1}0\}$ peaks exhibited various in-plane orientations at each position, with epitaxial relationships of 0°, 30°, and 11° with respect to graphene.

Figure 4.4 | Moiré fringes (patterns) observed within ZnO clusters (or grains) during the coalescence process. a, HR-TEM image showing rotational Moiré patterns between two different ZnO clusters with a rotation angle of 11.4°. Insets 1, 2, and 3 are corresponding FFTs obtained from Regions 1, 2, and 3. **b,** Higher magnification BF image of Fig. 4.2e. Moiré fringes are clearly shown within the ZnO clusters located on the underlying pre-formed ZnO layers. The Moiré fringes are marked with yellow arrows, and their spacing is ~ 12.1 Å. **c,** HR-TEM image of the grain boundary for ZnO grown for 10 min. The defective shape of the grain boundary, on the order of a few nanometers wide, is revealed. Moiré fringes marked with arrows are also observed along the grain boundary, with a spacing of ~7.8 Å. Insets 1, 2, and 3 are corresponding FFTs obtained from Regions 1, 2, and 3.

4.3 Crystal structure of ZnO in the initial stage of growth

4.3.1 Formation of rocksalt ZnO structure

The use of graphene as a substrate facilitated atomic-resolution imaging by minimizing the background signal from the underlying graphene and allowed more detailed investigation into the initial growth behavior. First, we focused on the nucleation stage, when little information was available through SAED, to inspect the crystallographic properties of individual nuclei. ZnO nuclei grown for 10 s mostly had rounded shapes and incomplete crystallized atomic arrangements. Surprisingly, ZnO nuclei with a cubic rocksalt structure were frequently observed, whereas ZnO nuclei with a hexagonal wurtzite structure were not observed (Fig. 4.5a). All of the rocksalt ZnO nuclei grew along the ⟨110⟩ direction, as confirmed by FFTs (inset of Fig. 4.5a). In contrast, as shown in Fig. 4.5b, the 1-min-grown ZnO nuclei with a hexagonal-faceted shape did not exhibit a rocksalt structure, but only a wurtzite structure along the ⟨0001⟩ direction (inset of Fig. 4.5b).

It was quite surprising that the rocksalt ZnO structure appeared during the initial growth; in previous studies, this structure occurred only under specific growth conditions, for example, under extremely high pressure[49] or with a cubic substrate[50]. The rare appearance of the rocksalt structure is attributed to the structural stability of the alternating form, *i.e*., wurtzite ZnO,

51

compared with the metastable rocksalt ZnO form. The instability of the rocksalt structures was confirmed by first-principles calculations that gave the total energies per unit cell of –36.16 and –34.97 eV for the wurtzite and rocksalt structures, respectively (Table 4.1, the total energy of the wurtzite structures was multiplied by a factor of two to compare with that of the rocksalt structures). GaN having smaller energy difference between the wurtzite and zincblende structures than that of ZnO was also given in Table 4.1 to highlight a smaller probability of cubic ZnO structure formation during the growth process.

The transformational behavior of rocksalt ZnO into wurtzite ZnO was further investigated. After the growth of ZnO on graphene for 10 s, the sample was kept in an MOCVD reactor for another 6 min at the same growth temperature without precursor gas. Figure 4.5c shows that the size of the ZnO nucleus remained the same as that of the 10-s-grown nucleus. However, all of the rocksalt ZnO structure had disappeared, and only the nuclei with the wurtzite structure and well-defined facets were observed, as was the case for ZnO growth after 1 min (Fig. 4.5b). This result demonstrates that the rocksalt phase of ZnO, when provided with sufficient time and energy, transforms into the more thermodynamically stable wurtzite phase.

4.3.2 Nucleation barrier in heteroepitaxial growth

The experimental findings in 4.3.1 explain the appearance of the metastable rocksalt ZnO structure in the early growth stages, in conjunction with the kinetics of nucleation. In the heterogeneous nucleation procedure, the embryo that overcomes the nucleation barrier only contributes to the formation of nuclei on the substrates, suggesting that the height of the nucleation barrier is a critical factor in the nucleation process.[51,52] For an early growth stage, the interfacial energy becomes a predominant factor determining the nucleation barrier of the initial stage due to the relatively large interfacial area-to-volume ratio of the nanomaterial. The interfacial energy strongly depends on the lattice match at the interface, and the kinetic energy barrier is proportional to the interfacial energy in the case of epitaxial growth.[51,52]

When the energy barrier for a metastable structure is much lower than that for a stable structure, then the transition to the metastable state can be prevalent during the initial growth stage. As illustrated in Fig. 4.5d, the rocksalt ZnO showed nearly a 1:1 and 4:5 lattice match along the X and Y directions, respectively, whereas wurtzite ZnO exhibited a 3:4 lattice match along both directions. This suggests better lattice matching at the interface between rocksalt ZnO and graphene, compared with that between wurtzite ZnO and graphene, as well as a lower nucleation energy barrier for the rocksalt ZnO. This lower nucleation energy barrier can preferentially lead to the formation of

the metastable rocksalt ZnO as an intermediate state.
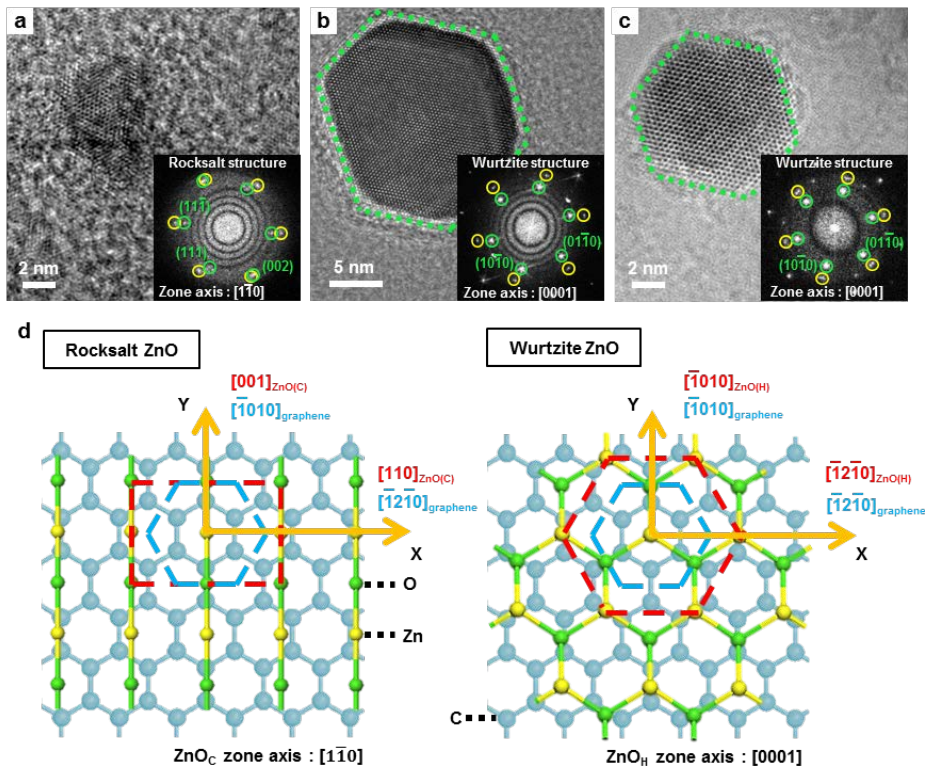
Figure 4.5 | Crystal structure transition of the ZnO nucleus from cubic to hexagonal in the early growth stage. a,b, HR-TEM images of each ZnO nucleus obtained for growth times of (a) 10 s and (b) 1 min. **c,** HR-TEM image of ZnO grown for 10 s, the same as a, and left in a reactor for another 6 min afterward without injecting diethylzinc gas. The corresponding FFTs and zone axes are provided in each figure. In the insets, the diffraction peaks of ZnO and graphene are marked with green and yellow circles, respectively. **d,** Epitaxial relationships between rocksalt/wurtzite ZnO and graphene, illustrated using a ball-and-stick model. The carbon, oxygen, and zinc atoms are represented by

55

blue, green, and yellow balls, respectively. Both rocksalt and wurtzite structures are placed on a basal plane of graphene, and their projected unit cells, along with their zone axes, are identified in the figure with red and blue dashed lines. The epitaxial relationships of ZnO $[001]_c$ ∥ graphene $[\bar{1}010]_h$ and ZnO $[110]_c$ ∥ graphene $[\bar{1}2\bar{1}0]_h$ in the case of cubic ZnO, and ZnO $[\bar{1}010]_h$ ∥ graphene $[\bar{1}010]_h$ and ZnO $[\bar{1}2\bar{1}0]_h$ ∥ graphene $[\bar{1}2\bar{1}0]_h$ in the case of hexagonal ZnO, are shown.

	Wurtzite [eV]	Zincblende [eV]	Rocksalt [eV]
GaN	−24.519	−49.002	−45.092
ZnO	−18.078	−36.102	−34.970

Table 4.1 | Total energy per unit cell for ZnO and GaN polymorphs (wurtzite, zincblende, and rocksalt). The calculated energies were obtained after complete structural optimization within the DFT framework using the generalized gradient approximation. The unit cell of wurtzite contains four atoms (two anions and two cations), whereas those of zincblende and rocksalt contain eight atoms (four anions and four cations); thus, the total energy of wurtzite should be multiplied by a factor of two when compared with that of zincblende and rocksalt.

4.4 Disorder in the atomic arrangements around defects

We further investigated various kinds of defects in 10- and 15-min-grown ZnO grains. Fig. 4.6a and b reveal low-magnification BF images showing extensively coalesced ZnO grains and various types of interfaces, including low-angle (indicated by dashed lines) and high-angle grain boundaries, which were not observed in the earlier growth stages. Distinct features of such grain boundaries, related to their atomic configurations, could be clearly observed on graphene using HR-TEM. The low-angle grain boundaries showed misorientation angles of less than 13°, and zigzag atomic configurations, retaining the $\{10\bar{1}0\}$ facets of ZnO at the boundaries, were commonly observed (Fig. 4.6c). The formation of step-like [0001]-tilt boundaries incorporating stable $\{10\bar{1}0\}$ ZnO planes rather than straight boundaries with high-index planes reduces their formation energy.[53,54]

Strong contrast resulting from local strain fields at periodic dislocation cores was also observed along the low-angle grain boundaries in Fig. 4.6d. When the misorientation angle was low (less than 10–15°), the distortion at the boundary was entirely accommodated by the inclusion of dislocations in the boundary. In the case of a pure-tilt boundary, the dislocation was edge-type, which essentially generated an extra half-plane of atoms. The edge component of the dislocation was confirmed by a Burgers circuit around a dislocation core

58

consisting of a low-angle grain boundary (Fig. 4.7a). The Burgers vector, identified with a yellow arrow, was found to be $\boldsymbol{b} = 1/3\langle11\bar{2}0\rangle$, the normal direction to the dislocation line.

In addition to the low-angle grain boundaries, high-angle grain boundaries having rotation angles greater than 20° were formed in the graphene-grown ZnO nanomaterials. The HR-TEM image in Fig. 4.6e shows that structural units appeared periodically at every third atomic spacing along the boundary denoted by the arrows. These periodic quadrilaterals containing bright spots along the boundary, marked with the dashed line, are clearly visible in magnified HR-TEM image (Fig. 4.7b). More importantly, all the high-angle grain boundaries observed in the ZnO nanomaterials grown on graphene were symmetric and exhibited misorientation angles of 21−24°. These characteristics of the high-angle grain boundaries are typically observed at the Σ7 boundary constituting the $\{12\bar{3}0\}$ plane, one of the coincidence site lattice (CSL) boundaries.[55] This is a special boundary which is usually formed to reduce the high-angle grain boundary energy and exhibits various atomic configurations, depending on the misorientation angle and the boundary plane.[55] In the ZnO/graphene system developed here, Σ7 boundaries with a $\{12\bar{3}0\}$ boundary plane were mostly observed. This boundary features the smallest periodicity of structural units among the possible tilt-grain boundaries in the hexagonal

59

system.

We also investigated threading dislocations within the grains. Strong contrast was shown in the BF images, indicating the presence of threading dislocations (Fig. 4.6f). The HR-TEM image in Fig. 4.6f shows that the dislocation did not distort the surrounding in-plane atomic arrangements, which is further confirmed by the construction of a closed Burgers circuit around the dislocation core in Fig. 4.7c. This suggests that the dislocation core had no Burgers vector component in the plane perpendicular to the vertical dislocation line, indicating that this threading dislocation is screw-type. In contrast, the edge-type threading dislocation showing in-plane disorder in the atomic arrangements were also observed within the grains (Fig. 4.7d). Burgers circuit drawn around the dislocation core revealed a Burgers vector of $b = 1/3\langle11\bar{2}0\rangle$, indicated by the yellow arrow. The distortion of the atomic arrangement was generated by inclusion of an extra half-plane of atoms in the perfect crystal.
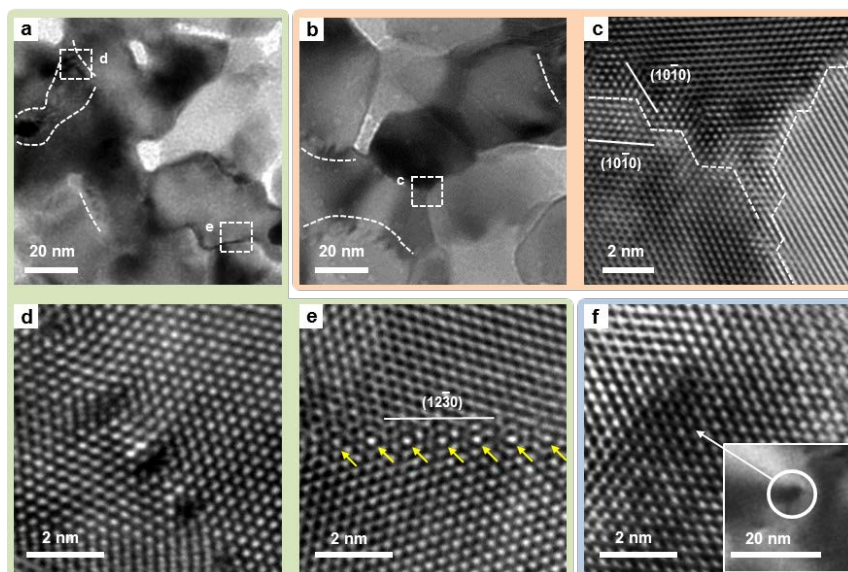
Figure 4.6 | Various kinds of defects generated during nanomaterial growth.
a,b, BF images obtained in the region where ZnO grains had substantially coalesced. The dashed lines in a and b denote low-angle grain boundaries. HR-TEM images were taken at each marked region, clearly showing the atomic configurations of various defects. **c,** Low-angle grain boundaries with well-developed $\{10\bar{1}0\}$ facets of ZnO, as identified with dashed lines. **d,** Low-angle grain boundary containing an array of edge-type dislocation cores. The boundary has a rotation angle of 7.1°. **e,** High-angle grain boundary with a rotation angle of 22.6° and the $\{12\bar{3}0\}$ boundary plane. Dislocation-like structural units periodically shown along the boundary are denoted by arrows. **f,** HR-TEM image of a screw-type threading dislocation observed within the grain. The inset shows the BF image of this threading dislocation. Edge-type threading dislocations are also presented in Fig. 4.7d.

61
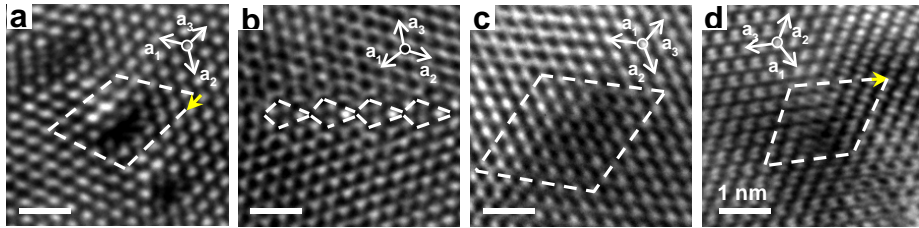
Figure 4.7 | Distortion of atomic arrangements near various defects. a, Enlarged HR-TEM image of Fig. 4.6d. The Burgers circuit is drawn around the dislocation core at the low-angle grain boundary, which reveals a Burgers vector of $b = 1/3\langle 11\bar{2}0\rangle$. **b,** Enlarged HR-TEM image of Fig. 4.6e. The quadrilaterals representing structural units are marked along the high-angle grain boundary plane of $\{12\bar{3}0\}$. The periodicity of the structural unit is well represented in the figure. **c,** Enlarged HR-TEM image of Fig. 4.6f. The Burgers circuit is drawn around a threading dislocation core; it forms a closed circuit, indicating no distortion in the atomic arrangement. **d,** HR-TEM image obtained from an edge-type threading dislocation. The Burgers circuit is also drawn around the dislocation core, which reveals a Burgers vector of $b = 1/3\langle 11\bar{2}0\rangle$. The directions a_1, a_2, and a_3 in the figures are hexagonal lattice vectors, and the yellow arrows denote the Burgers vectors of the defects.

62

4.5 Diverse applicability of the experimental technique for the initial growth study: ZnO nanomaterials on *h*-BN

4.5.1 Hexagonal boron nitride

Boron nitride (BN) is a chemical compound which is composed of equal numbers of B and N atoms bound each other. BN is isoelectronic to carbon-based materials, such as graphite, diamond, and carbon nanotube and, therefore, has crystal structures similar to their polymorphs; hexagonal form analogous to graphite has honeycomb lattice and layered structures (Fig. 4.8a, left side), sphalerite form corresponding to diamond consists of tetrahedrally coordinated B and N atoms (Fig. 4.8a, right side), nanotube form analogous to carbon nanotube is cylindrical nanostructure composed of alternating B and N atoms. Among these BN structures, hexagonal form is mostly found in nature since it is energetically the most stable phase. Meanwhile, one-atom thick layer of hexagonal BN (*h*-BN) analogous to graphene has recently attracted many interests in various research areas. Within its layer, B and N atoms are bound by strong covalent bonds, and the bond angle (B-N-B or N-B-N) is 120˚ that is expected for perfect hexagonal crystal structure, as shown in Fig. 4.8b.

Few layers of *h*-BN have been experimentally isolated by mechanical exfoliation method, as used in graphene production, or synthesized by CVD and pyrolysis method using appropriate chemical precursors. Figure 4.8c shows

few layers *h*-BN exfoliated from dispersed BN compounds in a common solvent.[56] The *h*-BN obtained from the exfoliation method mostly exhibits single-crystalline characteristics, as confirmed by HR-TEM images and corresponding FFT pattern in Fig. 4.8d.

In terms of electrical properties, *h*-BN is considered to be an insulator. *h*-BN has a wide band gap of ~5.2 eV in the range of UV light whereas graphene does not have band gap in common, the reason of its metallic characteristic. Because of this wide band gap, *h*-BN is transparent to visible light and colorless in nature and, therefore, sometimes called 'white graphene'. Insulating *h*-BN has also high dielectric breakdown strength of ~35 kV mm-1, indicating that it is highly promising as an extremely thin gate dielectric material.

Excellent thermal and chemical stability of *h*-BN also allows it to be widely used as parts of high-temperature equipment. Bulk *h*-BN ceramic is stable to decomposition at extremely high temperatures, up to 1000 °C in air, 1400 °C in vacuum, and 2800 °C in an inert atmosphere.[57] In addition, the reactivity of *h*-BN with other materials, including common solids and acids, is almost negligible. Such remarkable properties of *h*-BN make it suitable for construction of e.g. bearings and in steelmaking.[57]

4.5.2 Initial growth behavior of ZnO nanomaterials on *h*-BN

The experimental method used in this study can be expanded further to investigate the growth behavior of various materials on various 2-D layered materials. We briefly introduce the initial growth behavior of ZnO nanomaterials on h-BN, as an alternative 2-D material of graphene, to highlight the broad availability of this experimental method. ZnO was directly grown on h-BN lying on TEM grid by the same method as described in chapter 3.3. Detailed growth conditions of ZnO nanomaterials are given in Table 4.2.

Figure 4.9 shows morphological evolution of ZnO nanomaterials on oxygen plasma-treated h-BN (upper row) and on pristine h-BN (lower row) at the initial growth stages. Each image in Fig. 4.9 was taken from the specimen grown for 10 s, 1 min, 2 min, and 5 min, respectively. ZnO nanomaterials grew in both density and size as the growth proceeded, which was the same as observed for those grown on graphene. However, the size of nuclei (or clusters) was smaller than that grown on graphene; even though small nuclei were incessantly created over the whole area, their size was only about a few tens of nanometers and coalescence between the clusters was hardly taken place even for the specimens experiencing oxygen plasma treatment. There was no big difference in the size and density of ZnO clusters grown on oxygen plasma-treated h-BN from those on pristine h-BN as shown in upper and lower row in Fig. 4.9. This indicates that surface treatment on h-BN hardly affect the ZnO

growth, compared to the ZnO nanomaterials grown on graphene. Such a different behavior of ZnO growth might be attributed to lower reactivity of h-BN with respect to oxygen plasma treatment.

Orientational relationship between ZnO clusters at the early stages was also investigated using FFT patterns. HR-TEM image of 2-min-grown ZnO was taken (Fig. 4.10a), and corresponding FFTs were obtained from different ZnO clusters (Fig. 4.10b-e). Six-fold diffraction peaks in FFT patterns represent ZnO $\{10\bar{1}0\}$ planes taken along [0001] zone axis. These diffraction patterns were different at each cluster, indicating the clusters have different in-plane orientations. This is the same result as the initial state of ZnO nanomaterials grown on graphene.

Atomic-resolution observation could be also achieved by using h-BN as both a substrate and supporting layer. Extremely thin h-BN allowed various atomic-resolution images to be obtained, as represented in Fig. 4.11. These HR-TEM images show the agglomeration of two clusters having different in-plane orientations, indicated by two arrows in the figures. The coalescence among small ZnO clusters was observed in many places regardless of the surface treatment on h-BN. This is the same result as the case of ZnO grown on graphene even though the size of these clusters were much smaller than those grown on h-BN.

66

This brief investigation using *h*-BN told us the general growth behavior of nanomaterials as already described in chapter 4 in detail, including the morphological evolution, non-epitaxial growth, and coalescence of nanomaterials in the early growth stages. The only difference between the use of graphene and *h*-BN was the growth rate of ZnO nanomaterials at the early stages; ZnO grown on graphene grew faster and the size of these nuclei (or clusters) was larger than that grown on *h*-BN. This explicitly reveals that the growth is generally affected by the substrate, thus the study on the effect of different 2-D materials on the nanomaterial growth can be achieved using the experimental method demonstrated here.
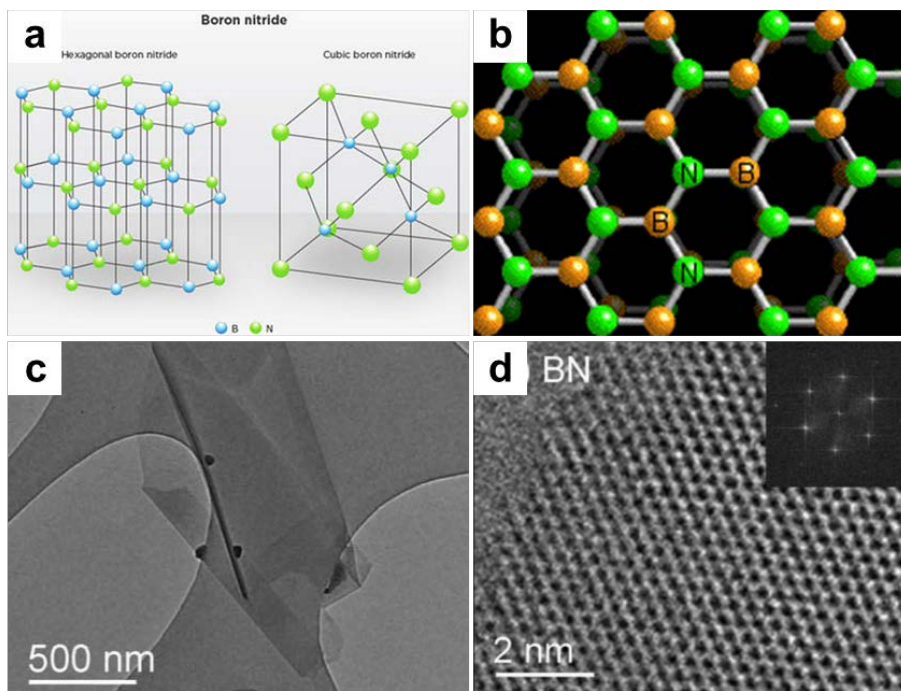
Figure 4.8 | The characteristics of BN. a, Crystal structures of BN; left side for *h*-BN and right side for cubic BN. **b,** Crystal structure of monolayer *h*-BN composed of alternating B and N atoms. **c,** TEM image of few layers *h*-BN placed on amorphous carbon layer.[56] **d,** HR-TEM image obtained from *h*-BN in c. Inset is a corresponding FFT pattern.[56]

	Growth conditions
Substrate	h-BN
Reactor pressure	~ 2 Torr
Growth temperature	600˚C
Growth time	10 s / 1 min / 2 min / 5 min
DEZn flow rate	20 sccm
DEZn dilute flow rate	40 sccm
O2 flow rate	100 sccm
Ar flow rate	1500 sccm
Bubbler temperature of DEZn	-10˚C

Table 4.2 | Typical growth conditions of ZnO nanomaterials on h-BN.
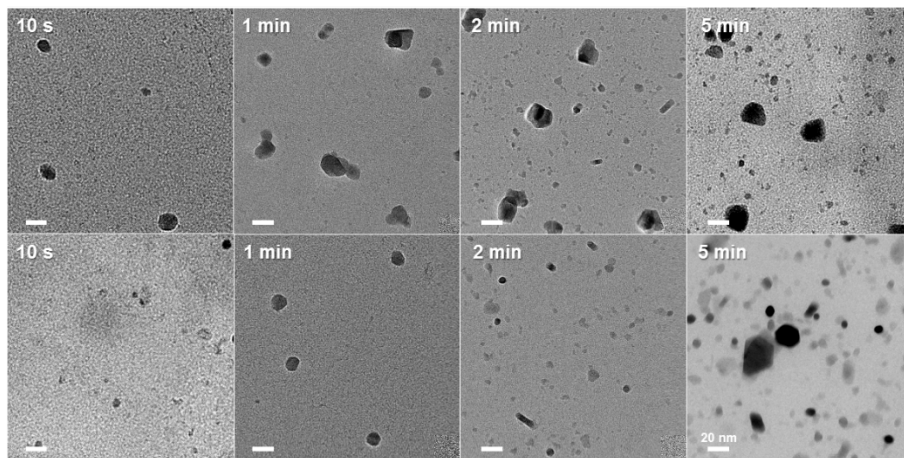
Figure 4.9 | Morphological evolution of ZnO nanomaterials on h-BN. BF images were obtained for ZnO grown on oxygen plasma-treated h-BN for 10 s, 1 min, 2 min, and 5 min, respectively, as indicated in the figures (upper row). ZnO was also grown on pristine h-BN at different growth times same as for that grown on oxygen plasma-treated h-BN (lower row).
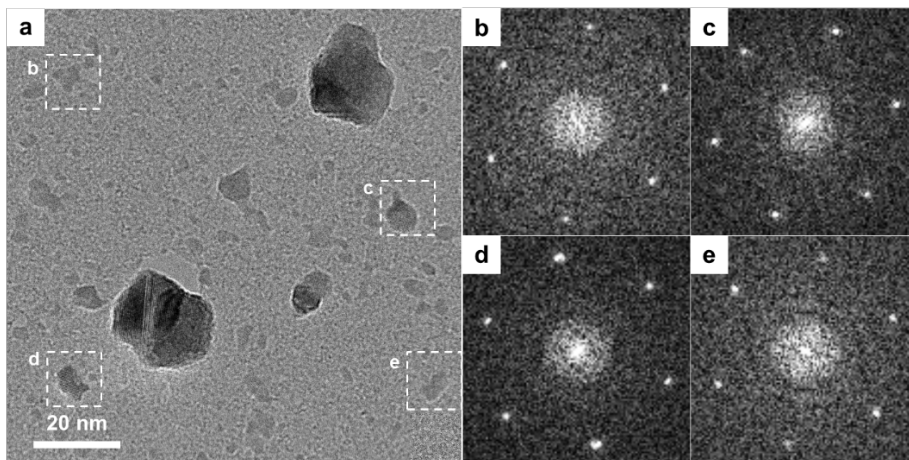
Figure 4.10 | Non-epitaxially grown ZnO clusters on *h*-BN in the initial growth stage. a, HR-TEM image of ZnO clusters grown for 2 min. **b-e,** FFTs were obtained from different ZnO clusters identified by dashed squares. The diffraction peaks in each FFTs represent ZnO $\{10\bar{1}0\}$ and they exhibited various in-plane orientations.
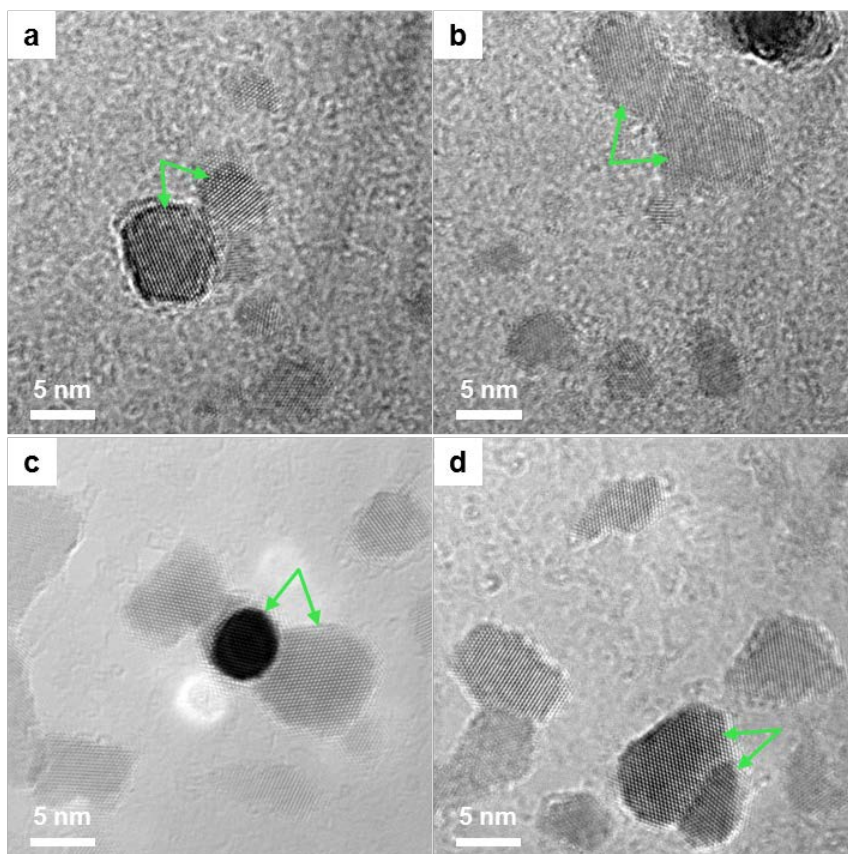
Figure 4.11 | HR-TEM images of ZnO nanocrystals agglomeration.
Nanocrystals grown (**a,b**) on oxygen plasma-treated *h*-BN and (**c,d**) on pristine
h-BN for 5 min were coalesced during the growth. Agglomerations of
nanocrystals with different in-plane orientations were marked with arrows in
the images.

Chapter 5. Conclusions

We demonstrated that various phenomena associated with nucleation and growth of nanomaterials on graphene can be visualized with high sensitivity and resolution by using graphene as both a substrate for nanomaterial growth and a supporting layer for TEM measurements. ZnO nuclei with uncommon cubic structures and non-epitaxially-grown ZnO clusters were observed in the early stage of growth, followed by evolution to large grains exhibiting an epitaxial relationship with graphene and formation of various defects. The experimental scheme demonstrated in this report enables the study of the initial growth mechanism of diverse nanomaterials on 2-D layered materials with atomic-resolution. More generally, we believe that this method offers great potential to enhance our knowledge of numerous behavior in materials science, where atomic-scale imaging with high sensitivity is required for fundamental understanding of the phenomena involved.

References

1 Yi, G. C., Wang, C. R. & Park, W. I. ZnO nanorods: synthesis, characterization and applications. *Semicond. Sci. Tech.* **20**, S22-S34 (2005).

2 Wang, Z. L. & Song, J. H. Piezoelectric nanogenerators based on zinc oxide nanowire arrays. *Science* **312**, 242-246 (2006).

3 Ju, S. Y. *et al.* Fabrication of fully transparent nanowire transistors for transparent and flexible electronics. *Nat. Nanotechnol.* **2**, 378-384 (2007).

4 Lee, C. H. *et al.* Flexible Inorganic Nanostructure Light-Emitting Diodes Fabricated on Graphene Films. *Adv. Mater.* **23**, 4614-4619 (2011).

5 Son, D. I. *et al.* Emissive ZnO-graphene quantum dots for white-light-emitting diodes. *Nat. Nanotechnol.* **7**, 465-471 (2012).

6 Lu, X. M., Rycenga, M., Skrabalak, S. E., Wiley, B. & Xia, Y. N. Chemical Synthesis of Novel Plasmonic Nanoparticles. *Annu. Rev. Phys. Chem.* **60**, 167-192 (2009).

7 Cibert, J. *et al.* Optically Detected Carrier Confinement to One and Zero Dimension in Gaas Quantum-Well Wires and Boxes. *Appl. Phys. Lett.* **49**, 1275-1277 (1986).

8 Zhuang, L., Guo, L. J. & Chou, S. Y. Silicon single-electron quantum-dot transistor switch operating at room temperature. *Appl. Phys. Lett.* **72**, 1205-1207 (1998).

9   Johnson, S. M. *et al.* Effect of Dislocations on the Electrical and Optical-Properties of Long-Wavelength Infrared Hgcdte Photovoltaic Detectors. *J. Vac. Sci. Technol. B* **10**, 1499-1506 (1992).

10 Dahan, P. *et al.* Properties of the intermediately bound alpha-, beta- and gamma-excitons in ZnO : Cu. *J. Phys-Condens Mat.* **10**, 2007-2019 (1998).

11 Wu, X. H. *et al.* Dislocation generation in GaN heteroepitaxy. *J. Cryst. Growth* **189**, 231-243 (1998).

12 Kaiser, U., Muller, D. A., Grazul, J. L., Chuvilin, A. & Kawasaki, M. Direct observation of defect-mediated cluster nucleation. *Nat. Mater.* **1**, 102-105 (2002).

13 Kim, B. J. *et al.* Kinetics of Individual Nucleation Events Observed in Nanoscale Vapor-Liquid-Solid Growth. *Science* **322**, 1070-1073 (2008).

14 Helveg, S. *et al.* Atomic-scale imaging of carbon nanofibre growth. *Nature* **427**, 426-429 (2004).

15 Milliron, D. J. *et al.* Colloidal nanocrystal heterostructures with linear and branched topology. *Nature* **430**, 190-195 (2004).

16 Hofmann, S. *et al.* In situ observations of catalyst dynamics during surface-bound carbon nanotube nucleation. *Nano Lett.* **7**, 602-608 (2007).

17 Yuk, J. M. *et al.* High-Resolution EM of Colloidal Nanocrystal Growth Using Graphene Liquid Cells. *Science* **336**, 61-64 (2012).

18 Zuo, J. M. & Li, B. Q. Nanostructure evolution during cluster growth: Ag on H-terminated Si(111) surfaces. *Phys. Rev. Lett.* **88**, 255502 (2002).

19 Hornvonhoegen, M., Legoues, F. K., Copel, M., Reuter, M. C. & Tromp, R. M. Defect Self-Annihilation in Surfactant-Mediated Epitaxial-Growth. *Phys. Rev. Lett.* **67**, 1130-1133 (1991).

20 Jeong, J. S. & Lee, J. Y. Investigation of initial growth of ZnO nanowires and their growth mechanism. *Nanotechnology* **21**, (2010).

21 Ustarroz, J., Gupta, U., Hubin, A., Bals, S. & Terryn, H. Electrodeposition of Ag nanoparticles onto carbon coated TEM grids A direct approach to study early stages of nucleation. *Electrochem. Commun.* **12**, 1706-1709 (2010).

22 Choi, J., Lee, H. & Kim, S. Atomic-Scale Investigation of Epitaxial Graphene Grown on 6H-SiC(0001) Using Scanning Tunneling Microscopy and Spectroscopy. *J. Phys. Chem. C* **114**, 13344-13348 (2010).

23 Wang, Z. L. Transmission electron microscopy of shape-controlled nanocrystals and their assemblies. *J. Phys. Chem. B* **104**, 1153-1175 (2000).

24 Hansen, P. L. *et al.* Atom-resolved imaging of dynamic shape changes in supported copper nanocrystals. *Science* **295**, 2053-2055 (2002).

25 McCaffrey, J. P., Phaneuf, M. W. & Madsen, L. D. Surface damage formation during ion-beam thinning of samples for transmission electron

microscopy. *Ultramicroscopy* **87**, 97-104 (2001).

26 Cheong, W. S., Hwang, N. M. & Yoon, D. Y. Observation of nanometer silicon clusters in the hot-filament CVD process. *J. Cryst. Growth* **204**, 52-61 (1999).

27 Grant, A. W., Hu, Q. H. & Kasemo, B. Transmission electron microscopy 'windows' for nanofabricated structures. *Nanotechnology* **15**, 1175-1181 (2004).

28 Enquist, F. & Spetz, A. The Fabrication of Amorphous Sio2 Substrates Suitable for Transmission Electron-Microscopy Studies of Ultrathin Polycrystalline Films. *Thin Solid Films* **145**, 99-104 (1986).

29 Kim, Y. J. *et al.* Position- and Morphology-Controlled ZnO Nanostructures Grown on Graphene Layers. *Adv. Mater.* **24**, 5565-5569 (2012).

30 Ozgur, U. *et al.* A comprehensive review of ZnO materials and devices. *J. Appl. Phys.* **98**, (2005).

31 Zhang, Y. F., Russo, R. E. & Mao, S. S. Quantum efficiency of ZnO nanowire nanolasers. *Appl. Phys. Lett.* **87**, (2005).

32 Park, W. I., Jun, Y. H., Jung, S. W. & Yi, G. C. Excitonic emissions observed in ZnO single crystal nanorods. *Appl. Phys. Lett.* **82**, 964-966 (2003).

33 Teke, A. *et al.* Excitonic fine structure and recombination dynamics in single-crystalline ZnO. *Phys. Rev. B* **70**, 195207 (2004).

34 Huang, M. H. *et al.* Room-temperature ultraviolet nanowire nanolasers. *Science* **292**, 1897-1899 (2001).

35 Novoselov, K. S. *et al.* Electric field effect in atomically thin carbon films. *Science* **306**, 666-669 (2004).

36 Lv, R. T. & Terrones, M. Towards new graphene materials: Doped graphene sheets and nanoribbons. *Mater. Lett.* **78**, 209-218 (2012).

37 Geim, A. K. & Novoselov, K. S. The rise of graphene. *Nat. Mater.* **6**, 183-191 (2007).

38 Lee, C., Wei, X. D., Kysar, J. W. & Hone, J. Measurement of the elastic properties and intrinsic strength of monolayer graphene. *Science* **321**, 385-388 (2008).

39 Verissimo, C., Gobbi, A. L. & Moshkalev, S. A. Synthesis of carbon nanotubes directly over TEM grids aiming the study of nucleation and growth mechanisms. *Appl. Surf. Sci.* **254**, 3890-3895 (2008).

40 Gu, G. *et al.* Growth of single-walled carbon nanotubes from microcontact-printed catalyst patterns on thin Si_3N_4 membranes. *Adv. Funct. Mater.* **11**, 295-298 (2001).

41 Zheng, H. M. *et al.* Observation of Single Colloidal Platinum Nanocrystal Growth Trajectories. *Science* **324**, 1309-1312 (2009).

42 Meyer, J. C. *et al.* The structure of suspended graphene sheets. *Nature* **446**,

60-63 (2007).

43 Meyer, J. C., Girit, C. O., Crommie, M. F. & Zettl, A. Imaging and dynamics of light atoms and molecules on graphene. *Nature* **454**, 319-322 (2008).

44 Lee, Z. *et al.* Direct Imaging of Soft-Hard Interfaces Enabled by Graphene. *Nano Lett.* **9**, 3365-3369 (2009).

45 Stoll, J. D. & Kolmakov, A. Electron transparent graphene windows for environmental scanning electron microscopy in liquids and dense gases. *Nanotechnology* **23**, 505704 (2012).

46 Novoselov, K. S. *et al.* Two-dimensional atomic crystals. *P. Natl. Acad. Sci. USA* **102**, 10451-10453 (2005).

47 Banfield, J. F., Welch, S. A., Zhang, H. Z., Ebert, T. T. & Penn, R. L. Aggregation-based crystal growth and microstructure development in natural iron oxyhydroxide biomineralization products. *Science* **289**, 751-754 (2000).

48 Herman, M. A., Richter, W. & Sitter, H. *Epitaxy : physical principles and technical implementation*. (Springer, 2004).

49 Bates, C. H., Roy, R. & White, W. B. New High-Pressure Polymorph of Zinc Oxide. *Science* **137**, 993 (1962).

50 Bobade, S. M. *et al.* A reconstruction of cubic rs-ZnO on MgO (200) substrate through (100) plane of w-ZnO:rs-ZnO for transparent electronic

79

application. *Appl. Phys. Lett.* **101**, 072102 (2012).

51 Kashchiev, D. *Nucleation : basic theory with applications*. (Butterworth Heinemann, 2000).

52 Liu, X. Y. Interfacial effect of molecules on nucleation kinetics. *J. Phys. Chem. B* **105**, 11550-11558 (2001).

53 Yuk, J. M. *et al.* Atomic structural variations of [0001]-tilt grain boundaries during ZnO grain growth occurred by thermal treatments. *Appl. Surf. Sci.* **257**, 4817-4820 (2011).

54 Diebold, U., Koplitz, L. V. & Dulub, O. Atomic-scale properties of low-index ZnO surfaces. *Appl. Surf. Sci.* **237**, 336-342 (2004).

55 Oba, F. *et al.* Atomic structure of [0001]-tilt grain boundaries in ZnO: A high-resolution TEM study of fiber-textured thin films. *Phys. Rev. B* **70**, 125415 (2004).

56 Coleman, J. N. *et al.* Two-Dimensional Nanosheets Produced by Liquid Exfoliation of Layered Materials. *Science* **331**, 568-571 (2011).

57 Engler, M., Lesniak, C., Damasch, R., Ruisinger, B. & Eichler, J. Hexagonal boron nitride (hBN) - Applications from metallurgy to cosmetics. *Cfi-Ceram. Forum Int.* **84**, E49-E53 (2007).

초   록

초기 핵생성과 그 성장과정을 연구하는 것은 재료공학 분야의 가장 큰 관심거리 중 하나이다. 초기 결정성장과정을 이해하고 제어하는 것은 산업적인 측면에서 봤을 때 우리가 원하는 특성을 발현하는 나노소재를 만드는 데 있어 필수적인 요소라고 할 수 있다. 결국, 초기 성장과정에서 생성된 핵이나 구조적 결함에서 발견되는 원자배열의 특성 등의 초기 결정성장단계의 중요한 요소들을 분석하기 위해서는 원자단위의 분해능을 활용한 연구가 꼭 필요하다. 이런 고분해능 이미징 기법은 지금까지 주로 결정학적인 정보를 함께 알려줄 수 있다는 장점이 있는 투과전자현미경을 이용하여 구현되어 왔다. 본 연구에서는 이 투과전자현미경을 이용하여 그래핀 위에 바로 성장된 나노물질의 초기 결정성장단계를 파악할 것이다. 매우 높은 전자빔 투과도와 기계적 강도를 자랑하는 그래핀은 전자빔의 산란에 의한 백그라운드 신호를 최소화하고 나노물질을 잘 지탱할 수 있다. 이런 특성들로 인해 그래핀은 투과전자현미경 분석에 있어 이상적인 지지대로 활용될 수 있다. 더불어 그래핀은 결정성이 있기 때문에 나노물질 성장에 있어서 기판으로도 활용될 수 있다. 이렇게 투명하고 결정성이 있는 그래핀은 나노물질을 그 위에 바로 성장시켜 관찰할 수 있다는 장점이 있고, 이는 초기 결정성장 단계를 어떤 다른 공정 없이 효율적으로 분석할 수 있는 요소로 작용한다.

본 연구에서는 위와 같은 그래핀의 장점을 활용하여 산화아연 나노물질의 초기 성장단계를 관찰하였다. 이 과정에서 산화아연 핵들이 초기에 결정구조가 바뀌는 것과 성장 시간에 따라 그래핀과 산화아연 사이의 결정방위 관계 역시 바뀌는 현상을 발견하였다. 또한, 나노물질 성장 중 다양한 형태의 결정결함이 생성되는 현상도 투과전자현미경의 고분해능 이미지를 이용하여 관찰할 수 있었다. 본 연구에서 사용된 새로운 기법은 이 연구에만 국한된 것이 아니라, 다양한 이차원 물질 위에서 다양한 나노물질들의 초기결정성장 과정을 관찰하고 연구하는데 활용될 수 있다는 장점이 있다.